Transport properties of concrete after drying-wetting regimes to elucidate the effects of moisture content, hysteresis and microcracking

Z. Wu, H.S. Wong* and N.R. Buenfeld

Concrete Durability Group, Department of Civil and Environmental Engineering, Imperial College London, UK

Abstract

Drying and wetting induce a number of microstructural changes that could impact transport properties and durability of concrete structures, but their significance is not well-established. This research examines pastes, mortars and concretes with different w/b ratios, binders, aggregate sizes, curing and conditioning regimes. 50 mm thick samples were dried to equilibrium at either 105°C, 50°C / 7% RH, 21°C / 33% RH or gentle stepwise at 21°C / 93% RH → 3% RH, and then rewetted stepwise by humidification at 21°C / 33% RH → 86% RH and full saturation to produce varying degrees of damage and moisture content. Oxygen diffusivity and permeability, electrical conductivity, microcracking, accessible and total porosity were measured at different conditioning stages over 3-year period to better understand the effects of shrinkage, hysteresis and drying-induced damage on transport properties. The effect of supplementary cementitious materials (GGBS, SF) and implications of drying-wetting on concrete durability are discussed.

Keywords: Shrinkage (C); Microcracks (B); Transport properties (C); Durability (C); Hysteresis; Drying-Wetting (A)

1. Introduction

Durability of concrete and concrete structures is not only dependent on proper selection of ingredients, mix design and site execution (placement, compaction, curing), but also on its interactions with the exposure environment. All degradation processes affecting concrete with the exception of mechanical damage involve the transport of ions and/or fluids through its porous microstructure. Therefore, durability of concrete depends largely on its ability to resist penetration of water and other aggressive species (chlorides, CO_2, oxygen, sulphates), with the main transport mechanisms being diffusion, permeation, electro-migration (conductivity) and capillary sorption. Understanding how microstructure influences these transport processes is absolutely critical for the development of more durable and sustainable concretes, and for reliable service-life management of structures.

Most structures in service experience substantial drying-wetting and temperature cycles. Consequently, concrete structures are rarely completely dried or fully saturated or in a state of constant and uniform hygrothermal conditions. Exposure to natural environments induces a number of important effects. For example, drying leads to removal of water from pores and hydrates, and consequent volumetric shrinkage and microcracking [1-12]. On rewetting, the microstructure regains water and swells. However, some of the changes that occurred on first drying are non-reversible [13, 14]. The moisture state (which can be represented as moisture content, degree of saturation or equilibrium relative humidity) influences the type and rate of transport processes [9, 15-18]. It is also well-known that cyclic drying-wetting induces sorption hysteresis where the hygral state of cementitious materials exhibits a complex path (history) dependent behaviour [19-21].

All these effects may impact transport processes and durability, but their relative contribution or significance is not well-established. This is partly because they occur simultaneously and it is very challenging to decouple/isolate them to enable a systematic study. Furthermore, the associated experiments are extremely

* Corresponding author. Tel: +44 20 7594 5956, E-mail: hong.wong@imperial.ac.uk

time-consuming due to the slow processes involved, particularly for a representative (thick) sample. Cracks smaller than 0.1 mm, i.e. "microcracks" are of particular interest because it is very difficult to control and eliminate them by proper structural design and use of steel reinforcement [22]. One particular aspect that remains unclear is the importance of microcracking and other drying-induced microstructural changes on transport properties when cementitious materials undergo drying-wetting cycles. Very few studies have examined this and where available, they involve mainly dried pastes and mortars rewetted to fully saturated condition and tested for water permeability [2, 23-25]. Studies on how moisture hysteresis influences transport properties of concrete, in particular those concretes containing supplementary cementitious materials (SCMs), are also lacking [20, 26, 27]. Furthermore, most studies have been carried out on small (crushed) or thin samples (to accelerate moisture equilibrium), but thin samples can be dried with little microcracking [7, 28] and are not representative of typical concrete cover in real structures.

This paper presents an attempt to isolate and to better understand some of these effects by subjecting a range of pastes, mortars and concrete samples to several drying regimes (105°C, 50°C / 7% RH, 21°C / 33% RH or stepwise at 21°C / 93% RH → 3% RH) to induce varying degrees of damage and moisture content. The micro-cracked samples were then reconditioned at gradually increasing relative humidity (21°C / 33% RH → 86% RH) and to full saturation. Oxygen diffusivity and permeability, moisture content, degree of saturation and accessible porosity were measured at various stages of each conditioning regime. Electrical conductivity and total porosity were determined at saturation. Microcracking was characterised using fluorescence microscopy and image analysis. The entire programme involved more than 1440 transport measurements over a 3-year period. The questions that we wish to answer include: a) What is the nature of drying-induced microcracking? b) To what extent microcracks influence transport properties after accounting for moisture effects? c) What are the effects of moisture hysteresis on transport properties? and d) How do systems containing SCMs behave compared to those containing CEM I?

2. Experimental

2.1 Materials

The binders used were ordinary Portland cement CEM I 32.5 R, CEM III/B 42.5 N containing 70% ground granulated blastfurnace slag (GGBS) and CEM I blended with 10% silica fume (SF). Oxide composition and loss on ignition of the CEM I, CEM III/B and SF are shown in Table 1. The mineral composition (Bogue) of CEM I was 52.7% C_3S, 19.3% C_2S, 10.6% C_3A, 7.4% C_4AF by mass. Specific gravities of the CEM I, CEM III/B and SF were 3.06, 2.90 and 2.30 respectively. The fineness of CEM I and CEM III/B were 290.5 m^2/kg and 463.5 m^2/kg respectively. CEM III was factory pre-blended while silica fume was added to CEM I during concrete batching.

A polycarboxylate-based superplasticiser at dosage of 0.5% wt. binder was used to improve the workability of the low water/binder (w/b 0.35) mixes. Thames Valley sand (< 5 mm) and crushed limestone (< 10 mm) were used as fine and coarse aggregates respectively. Limestone was selected as coarse aggregate because of its high stiffness and low shrinkage. This increases the aggregate/paste property contrast, the amount of aggregate restraint and therefore the potential for microcracking. Sieve analyses showed that the sand complied with BS 882:1992 medium grading while the limestone complied with BS EN 12620:2002+A1 overall grading. The specific gravity at saturated surface dry condition (SSD) and 24-hour water absorption were 2.54 and 0.52% for the sand, 2.71 and 0.88% for the limestone.

2.2 Samples

Eight concrete, mortar and paste mixes were prepared according to the mix proportions shown in Table 2. Mix proportioning was designed by absolute volume. The free water/binder (w/b) ratio was either 0.35 or 0.50, obtained by correcting batch water for aggregate absorption and water from the superplasticizer. Total aggregate volume fraction for concrete mixes was fixed at 68% to enable meaningful comparison between concretes. However, the mortars contained slightly lower aggregate volume fractions because of the difficulty in

compacting mortars with high sand content, in particular for the lower w/b mix. It was important to ensure that the mixes were well compacted, otherwise excess air voids would be another variable influencing mass transport properties.

128 disc samples of 100 mm diameter and 50 mm thickness were prepared and tested. The sample thickness was chosen as representative of the cover to steel reinforcement in concrete structures. Batching was carried out by dry mixing cement and aggregates for 30 s in a pan mixer, and then adding water (with superplasticizer if required) and mixed for a further 3 min. Samples were cast in steel moulds and compacted in two layers on a vibrating table until no significant release of air bubbles was observed. All mixes produced were easily compacted and showed no evidence of bleeding or segregation. Inevitably, the microstructure of the cast and trowelled surfaces will be different to that of the bulk material due to wall/packing effects, as would be the case in real structures. Given the thickness of samples tested, the effects of surface heterogeneity were probably small and insignificant and no attempt was made to isolate these.

2.3 Curing and conditioning

The compacted samples were covered with wet hessian fabric and plastic sheet at room temperature for the first 24 hours to prevent drying. Afterwards, samples were demoulded and sealed-cured at room temperature to ages of 3 and 90 days. Sealed curing was achieved by wrapping each sample with at least 6 layers of cling film and sealing in polythene bags. Periodic weighing of the sealed samples found no significant weight change. The estimated degree of hydration using the backscattered electron microscopy method for similar CEM I systems after sealed curing are 0.62 (3 days) and 0.84 (90 days) at w/b 0.5, and 0.63 (3 days) and 0.72 (90 days) at w/c 0.35 [29]. After curing, samples were unwrapped and subjected to four conditioning regimes to produce samples with varying degrees of microcracking and moisture content. Each regime consists of several drying and wetting stages as summarised in Fig. 1. Prior to conditioning, the curved side of each disc was sealed with two layers of waterproof tape to induce unidirectional drying. This was deemed to be a more realistic approximation to the way in which structures dry or wet in service.

Conditioning regime A was the least severe, involving gradual step-wise drying at 21°C from 93% RH to 86% RH, 76% RH, 66% RH, 55% RH, 33% RH and 3% RH. Regimes B, C and D were more severe and consisting of an initial drying stage at 21°C / 33% RH, 50°C / 7% RH and 105°C respectively. These produce samples with varying degrees of microcracking and moisture content. Subsequently, the dried samples were rewetted by humidification at gradual step-wise increase of relative humidity from 33% RH to 55% RH, 66% RH, 76% RH and 86% RH at 21°C, and finally full vacuum saturation. Saturated salt solutions were used to produce the required RH at 21°C. These were KNO_3 (93% RH), KCl (86% RH), NaCl (76% RH), $NaNO_3$ (66% RH), $Mg(NO_3)_2$ (55% RH) and $MgCl_2$ (33% RH) [30, 31]. Silica gel was used to achieve 3% RH. Conditioning was carried out in either an enclosed box in temperature controlled lab (± 1°C) or in an oven, both contained fans to circulate air and soda lime to avoid carbonation.

Samples were frequently weighed and tested for transport properties when mass equilibrium at each drying or wetting stage was achieved. Samples dried at 50°C and 105°C were cooled overnight to room temperature (21°C) in a vacuum desiccator containing silica gel prior to transport testing to prevent moisture uptake upon cooling. The mass before and after cooling were recorded and the difference was always less than 0.01%. Equilibrium was assumed when mass change was less than 0.01% per day. Samples were then moved to the next conditioning stage and the process repeated. The conditioning was very time-consuming, requiring up to 800 days for completion per sample.

2.4 Moisture content, degree of saturation and porosity

Sample mass was monitored throughout the curing and conditioning regimes using an electronic balance accurate to 0.01 g. From these measurements, five parameters relating to the moisture condition and porosity of the sample were obtained: the moisture content, degree of saturation, accessible porosity, total porosity and sorption or desorption coefficients. Moisture content (w) was calculated as mass of water contained in the sample (m) per mass of its 105°C oven-dried state (m_d), expressed as a percentage:

$$w = \left(\frac{m - m_d}{m_d} \right) \times 100\% \quad \textbf{Eq. 1}$$

Sorption (and desorption) coefficients were estimated from the slope of the best-fit linear regression between Δw (change in moisture content) against square-root of conditioning time. The coefficient of regression was greater than 0.95 in most cases. The degree of saturation (s) was calculated by dividing the moisture content at a particular conditioning stage by the moisture content at the vacuum saturated state, expressed as a percentage. This represents the percentage porosity filled with moisture (and hence inaccessible to gas transport):

$$s = \left(\frac{m - m_d}{m_s - m_d} \right) \times 100\% \quad \textbf{Eq. 2}$$

Where m_s is the mass at vacuum saturated and surface dry condition.

Accessible porosity ϕ is the volume fraction of empty pores and cracks. This was estimated from the mass difference between vacuum-saturated state and preconditioned state (i.e. mass at a particular conditioning stage shown in Fig. 1), divided by sample volume V. Here, the density of water ρ was taken to be 1 g/cm^3.

$$\phi = \left(\frac{m_s - m}{\rho V} \right) \times 100\% \quad \textbf{Eq. 3}$$

Total porosity ϕ_t was estimated from the mass difference between vacuum saturated state and 105°C oven-dried state, divided by the sample volume V.

$$\phi_t = \left(\frac{m_s - m_d}{\rho V} \right) \times 100\% \quad \textbf{Eq. 4}$$

We recognise that the choice for the "dry" reference state for calculating the above is important. We used 105°C dried state as the reference for the sake of convenience, repeatability and because the most severe regime (D) was dried to this level. In addition, 105°C drying is a widely used practice for obtaining the so-called "evaporable water" content e.g. RILEM TC 116-PCD [32], but it is also recognised that some hydrates will lose water at this level. Therefore, the calculated properties include a minor fraction of water held in gel pores and hydration products, in addition to free water in capillaries.

2.5 Mass transport properties

Three replicate samples were tested for oxygen diffusivity and oxygen permeability when they had achieved mass equilibrium at each drying or wetting stage (when mass change was less than 0.01% per day). Oxygen was used because it has negligible physical or chemical interaction with cementitious materials. Details of the test methods are given in [9]. The sample was fitted into a silicone rubber ring placed in a transport cell and the circumference sealed by applying 15 kN compression on the top of rubber ring, which expands and grips the sample at a lateral confining pressure of 0.57 MPa. The small confining pressure is sufficient to prevent side leakage without causing additional damage or crack closure [11].

Oxygen diffusivity was determined by exposing the two opposite flat faces of the sample to oxygen and nitrogen at the same pressure. The gasses counter-diffuse through the sample and the oxygen concentration in the outflow stream was measured at steady-state using a zirconia analyser to calculate diffusivity. Oxygen permeability was determined by placing the sample in a similar cell, applying gas pressure of 0.05, 0.15 and 0.25 MPa above atmospheric, and measuring the steady-state outflow rates at each pressure. The apparent permeability at each pressure was calculated according to Darcy's law for incompressible fluids and the intrinsic permeability was then determined by applying Klinkenberg's correction for gas slippage.

A particular concern was that the samples might undergo additional drying during testing so affecting its accuracy. Therefore, sample mass before and after testing was monitored, and in all cases showed negligible change. Another concern was that a moisture gradient might exist even when samples had apparently reached mass equilibrium and that this could influence results. We examined this by wrapping and sealing preconditioned

samples to allow moisture redistribution and retesting after several weeks. The results showed that the changes in transport properties were insignificant, indicating that the residual moisture gradient (if it exists) did not have an important influence.

At the end of each conditioning regime, samples were vacuum-saturated with water and tested for electrical conductivity. This was carried out by clamping the flat surfaces of the disc with two brass plate electrodes connected to an LCR databridge. A generous amount of a salt-free electrode gel was applied to ensure good electrical contact between the sample and electrodes. Resistance was then measured at an alternating current of 1 kHz frequency to minimise polarisation effects. Three measurements were taken per disc and averaged. Electrical conductivity was then calculated from the resistance and discs dimensions.

2.6 Microcrack characterisation

Fluorescence microscopy was used to characterise microcracking on selected samples dried at 21°C, 55% RH and 33% RH, 50°C and 105°C. Samples were first pressure-impregnated from the top flat surface with a low viscosity fluorescent-dyed epoxy in a cell similar to that used for gas permeability. Compressed air at 0.7 MPa was applied for 6 hours. The sample was then sectioned by diamond saw to extract an 8 mm thick slice through the centre, and ground using silicon carbide paper of grit sizes 80 and 120 to obtain a flat surface for imaging.

Imaging was carried out on the surface exposed to drying and on the cross-section perpendicular to this, allowing surface and internal microcracking to be characterised. A 24 MP digital SLR camera was used in a dark room under 15 W UV lamp to induce florescence. The camera was operated at low ISO, small aperture to increase depth of field and slow shutter speed to achieve adequate exposure. This gave a macro view for measuring epoxy penetration depth. Subsequently, a petrographic microscope (Olympus BX 51) operated in fluorescence mode was used for imaging at higher resolution. A large number of overlapping images were captured at 50× magnification (2048 ×1536 pixels, pixel size 0.89 μm). The images were then aligned and stitched to produce a high-resolution montage of the entire epoxy-intruded area.

The area fraction and depth of the epoxy intrusion, and characteristics of the microcracks were measured using image analysis on three replicate samples. The average epoxy intrusion depth was obtained by dividing the impregnated area by sample width. All detectable microcracks were carefully traced on the enlarged montage to obtain a binary image of the cracks. This procedure is very time-consuming, but required for accurate and statistically significant results. Subsequently, the number of microcracks, their orientation with respect to the exposed surface, crack density, width and length were measured using image analysis. Crack density was defined as the total length of microcracks divided by image area. Full details of the analysis are given in [11, 12].

3. Results

3.1 Transport properties after drying

Fig. 2 shows the average gas diffusivity and permeability of concretes, mortars and pastes after being subjected to drying to either 21ºC / 55% RH (stepwise), 21ºC / 33% RH, 50ºC 7% RH or 105ºC. Precision is expressed as standard error ($= \sigma/n^{1/2}$). Transport properties decrease with decrease in w/b ratio and increase in curing age, as expected. Mixes containing GGBS and SF gave the lowest transport coefficients, with SF performing marginally better (lower values). Their diffusivities were 50-70% lower than the equivalent mixes without SCM at the same w/b ratio, curing age and conditioning regime, while permeabilities were 34-80% lower. Paste P 0.5 and concrete C 0.5 gave the highest diffusivity and permeability respectively for all curing ages and drying regimes. Concretes tend to show higher than expected permeability compared to their counterpart pastes or mortars. This is due to greater amount of microcracking and size effects [12, 33].

The results clearly show that both diffusivity and permeability increase with severity of drying. Oven drying at 105ºC produced the highest transport coefficients for all cases while stepwise drying at 21ºC gave the lowest. Diffusivity after 105ºC drying was 2 to 18 times higher than that at 21ºC / 55% RH (stepwise), and up to 40% higher than at 50ºC. Permeability measured after 105ºC drying was 3 to 25 times higher than that at 21ºC 55% RH (stepwise) and up to 160% higher than at 50ºC. Therefore, drying induced a much larger change in transport

property compared to that achieved by varying the w/b (0.35 → 0.5), curing age (3 → 90 days) or addition of SCMs (GGBS, SF). A further observation is that drying induced a greater increase in transport for pastes, low w/b ratio, early-age samples and those with SCMs. The increase in transport could be due to microcracking (Section 3.2), but the exact relationship is complex because the different drying regimes produce different degrees of saturation (Section 3.3) that would also influence transport.

3.2 Drying-induced microcracking

Examples of sample cross-sections after epoxy impregnation and the epoxy intrusion depths are shown in Fig. 3a and 3b respectively. The average intrusion depth ranged from 0.1 mm to 6 mm. Epoxy penetration increased with drying and w/b ratio, but decreased with curing age or addition of SCMs. However, the penetration front is spatially variable as can be seen in Fig. 3a. Locations that showed large impregnation depths coincide with presence of microcracks that propagate deeper into the sample, viewable at higher magnification using fluorescence microscopy (Fig. 5). Therefore, the depth of impregnation is approximately correlated to the depth of microcracking. Concretes consistently showed the largest impregnation followed by mortars and pastes, for the same w/b ratio, curing age and drying regime.

Fig. 4 presents example binary images to highlight the microcracking on the exposed surface of pastes after drying. They show a map-cracking pattern with characteristic triple-branching morphology typical of shrinkage-induced microcracking [3, 5, 6-10]. The measured length and density of the surface microcracking are given in Table 3. A higher degree of microcracking was observed in samples with larger w/b ratio, subjected to a more severe drying regime and in concretes compared to pastes. Stepwise dried at 21°C samples also showed microcracking, but significantly less extensive compared to the other drying regimes. Microcrack length and density increased by a factor of ≈ 100 in 105°C dried samples when compared to stepwise drying at 21°C.

Fluorescence imaging on sample cross-section (Fig. 5) shows that the surface microcracks tend to propagate approximately perpendicular from the exposed surface to depths of several mm (< 10 mm) into the sample. The morphology of microcracks in mortar and concrete is influenced by aggregate particles, but shows very little tendency for branching. The cracks occur through the cement paste (matrix cracks) or along the aggregate-paste interface (bond cracks), propagating from one particle to a neighbouring particle where it is either arrested or travels around the aggregate particle. The microcracks rarely propagate through aggregate. As reported in an earlier publication on similar samples [12], the number, length and width of the microcracks increased with severity of drying. The widths ranged between 1 and 60 μm, but more than 80% of the microcracks have widths smaller than 10 μm and lengths shorter than 100 μm. The width, length and density of microcracks increased with increase in aggregate size for the same drying regime.

It should be noted that the observed microcracks are unlikely to have been caused by sample preparation, for example damage from cutting, grinding or polishing. This is due to the fact that samples were epoxy impregnated prior to any of these procedures. The epoxy fills in cracks and voids, and preserves these structures when epoxy is hardened. Furthermore, impregnation was not carried out under vacuum to avoid the possibility of additional drying induced cracking. If any new microcracks form during sample preparation, these would not be epoxy-filled and therefore not imaged with fluorescence microscopy. Thus, the detected microcracks must either be inherent or induced by the imposed drying regime, and they are interconnected to the exposed surface.

3.3 Water content and degree of saturation

Fig. 6 and Fig. 7 present the evolution of moisture content (Eq. 1) and degree of saturation (Eq. 2) for selected pastes and concretes when conditioned to the regimes indicated in Fig. 1. Results show that samples in Regime A undergo gradual continuous decrease in moisture content and saturation degree. In contrast, samples in Regimes B, C and D undergo an initial sharp decrease and then gradual increase in moisture content and saturation degree upon rewetting. As expected, drying at 105ºC (Regime D) produced the steepest mass loss rate followed by 50ºC (Regime C) and 21ºC 33% RH (Regime B). Although the water content curves (Fig. 6) exhibit similar trends to those of saturation degree (Fig. 7), they provide different information since the former indicates how much water remained in the sample while the latter indicates the pore fraction filled with water.

Water contents and degrees of saturation were higher in samples with larger w/b ratio and shorter curing age. Most samples (except for 0.5 w/b, 3-day cured) had saturation degrees much lower than 100% at the start of conditioning. This is due to the (sealed) curing induced self-desiccation, the effect being more severe at low w/b ratio and longer curing. Concretes and mortars showed similar trends to pastes. However, samples containing SCMs (SF and GGBS) had higher moisture contents and saturation degrees compared to samples with only CEM I. This can be explained by the fact that SCMs produce more C-S-H gel which refines the pore size distribution such that a higher fraction of moisture is retained at a given RH compared to CEM I systems. The water is held strongly by the C-S-H and is only removed on severe drying.

It is also interesting to note that despite having much lower moisture contents, concretes and mortars took about the same time to achieve mass equilibrium as pastes. This is further clarified by examining the desorption and sorption coefficients (%/day$^{0.5}$) in Table 4. The data show that rates of drying and re-wetting are influenced by w/b ratio, curing age and SCMs as would be expected. It can be seen that the values for concretes and mortars are much lower than pastes. Also, sorption coefficients are consistently much lower than the desorption coefficients. Interestingly, the sorption coefficients are not hugely affected by initial drying. Regardless of whether samples were initially dried at 105ºC, 50ºC or 21ºC 33% RH, they gained mass at approximately the same rate upon rewetting at step-wise increasing RH.

3.4 Moisture hysteresis

Fig. 8 shows the equilibrium moisture content vs. RH plots for various samples and conditioning regimes. These have very similar qualitative appearance to corresponding plots of saturation degree vs. RH (not shown), and the effects of w/b, curing age, aggregate and SCMs on the equilibrium moisture content can be seen. For the same RH, the equilibrium moisture contents on rewetting are lower than those on drying. Thus, significant moisture hysteresis occurs between desorption and sorption over the entire RH range. As expected, the hygral path (moisture history) strongly influences equilibrium moisture content and this is well-documented [e.g. 19-21]. Nevertheless, moisture content is restored upon vacuum saturation (100% RH) regardless of drying history.

It should be pointed out however, that the plots shown in Fig. 8 are not strictly water vapour desorption-sorption isotherms since the first data point for regimes C and D were measured at elevated temperatures (50°C, 105°C). Nevertheless, there are similarities. In conventional isotherms, hysteresis is most significant above 40% RH, where within this range capillary condensation and evaporation occur. Our data for regimes A and B (both measured at 21°C) are consistent with this. The equilibrium moisture content at 33% RH for Regimes A and B coincide for most samples except P 0.5-3d. There is no reason why P 0.5-3d should behave differently, therefore this departure could be an experimental error (e.g. sample preparation or testing error).

The differences in moisture content between equivalent (w/b, curing age) paste, mortar and concrete can be largely explained by the presence of dense, non-sorptive aggregates. This is verified in Fig. 9 where the moisture contents for concretes are expressed as fraction of cement content, and compared against those of pastes. Despite the huge variation in mix proportions and curing age, there is remarkably good agreement between the values for paste, concrete and mortar (not shown) once they are normalised to cement content. This shows that for the same binder type, w/b ratio and curing age, the amount of water remaining after equilibrium at a particular RH is approximately the same, in agreement with the observation in [19]. The presence of dense aggregate particles and the aggregate-paste "interfacial-transition zone" (ITZ) do not influence equilibrium moisture content or increase transport properties. In fact, aggregates decrease the desorption and sorption coefficients as shown in Table 4. This shows that the effects of dilution (decrease in total porosity) and increase in cement paste tortuosity outweighs that of the porous ITZ, consistent with earlier studies [33, 34].

3.5 Transport properties after drying and re-wetting

Oxygen diffusivity and permeability of various samples as they undergo drying and re-wetting are shown in Fig. 10 and Fig. 11 respectively. Results are plotted against conditioning RH. Overall, the measured transport properties ranged over 2 orders of magnitude: diffusivity from 3.0×10^{-9} to 6.4×10^{-7} m^2/s, and permeability from 6.8×10^{-18} to 6.7×10^{-16} m^2. These values are sensitive to changes in mix w/b ratio, curing age, aggregate content and presence of SCMs, and are consistent with previous measurements on similar samples [33, 35]. However, drying induced the largest change in transport. Diffusivity measured after drying at 105ºC was 4 to172

times greater than at 21ºC 86% RH. Permeability after 105ºC drying was 4 to 69 times higher than at 21ºC / 86% RH. The corresponding increase in transport after drying at 50°C relative to 21ºC / 86% RH was 3 to 56 times for diffusivity and 3 to 21 times for permeability. Drying caused the greatest increase in pastes, early age samples and samples containing SCMs. This is consistent with the observation that these samples lost the highest amount of water on drying (Fig. 6).

On re-wetting, transport properties for all samples decreased. However, the magnitude of change on re-wetting to 86% RH is modest compared to that on drying. Therefore, a hysteretical behaviour is observed between measurements made during drying and re-wetting. Nevertheless, when the transport data are re-plotted against degree of saturation (Eq. 2) as shown in Figs. 12-14, the apparent hysteresis is drastically reduced or disappears completely. In many cases, the data from different conditioning regimes show significant overlaps. Samples of the same mix composition and curing produced similar transport properties once conditioned to similar saturation degrees, despite the fact that they were subjected to different drying severity and had different degrees of microcracking (Section 3.4, Figs. 3 & 4) prior to re-wetting. This is particular evident for samples that were not exposed to oven drying (A, B). In some cases, oven-dried samples (C, D) show higher transport properties than gently dried (A, B) samples when comparison is made at equal saturation degree, i.e. where the curves cross-over. The largest of these are indicated by arrows in Figs. 12-14 and they range from 41% to 96% for diffusivity, and 54% to 354% for permeability. These represent the maximum "residual" effect of drying on transport properties after accounting for moisture content and their significance will be discussed later.

Fig. 15 plots transport properties vs. accessible porosity (i.e. empty porosity, Eq. 3) for all samples. Despite the wide range in mix composition, curing and conditioning regimes involved, a strong correlation is observed between diffusivity and accessible porosity. The correlation for permeability however, is much weaker with large scatter between mixes. Gas diffusion occurs due to concentration gradient where movement results from random collisions of gas molecules through empty pore space in the media. Therefore, gas diffusivity is strongly dependent on total volume of accessible pores (and cracks). In contrast, pressure-induced flow occurs preferentially through large interconnected pores and cracks that offer paths of least resistance. As such, permeability is not only dependent on accessible porosity, but also size distribution and higher order geometry such as tortuosity and connectivity. This explains the larger scatter seen in Fig. 15b.

3.6 Electrical conductivity and porosity after vacuum saturation

Fig. 16 shows the electrical conductivity and total porosity (Eq. 4) measured after samples were dried, re-wetted and vacuum saturated. Again, the measurements are sensitive to changes in w/b ratio, binder type and aggregate content. For example, the electrical conductivity of w/b 0.35 concretes was 30-60% lower compared to the 0.5 w/b concretes. Electrical conductivity is also a function of pore solution composition, which is likely to be different for different w/b ratio and binder type. Presence of SF and GGBS decreased conductivity by 60-80% compared to CEM I only concretes. These are consistent with the diffusivity results. Mortars had higher electrical conductivity and porosity than concretes due to their lower aggregate content. However, the drying regimes prior to vacuum saturation did not appear to have a strong and consistent effect on electrical conductivity or total porosity. In some cases, severely dried samples showed an increase in conductivity and porosity, but others did not. These trends are insignificant given the uncertainties in the measurements. Thus, one may conclude that any drying-induced damage or changes to the microstructure have little effect on electrical conductivity and total porosity once the samples are re-saturated in vacuum.

4. Discussion

4.1 Effects of drying and shrinkage

The large increase in transport observed on drying (Figs. 2, 10 & 11) is due to a number of microstructural changes. When dried from a saturated state, the largest pores tend to empty first followed by successively smaller pores, hence the volume and connectivity of pores accessible to gas transport increases. Sorption isotherms [19, 36] and ^{1}H NMR experiments [37] show that water residing in capillary pores empty at ≈ 85%

RH, corresponding to pores larger than ≈ 10 nm according to the Kelvin-Laplace equation. Gel pores within low-density (LD) C-S-H empty at ≈ 85% to 50% RH, and within high-density (HD) C-S-H at ≈ 50% to 25% RH. Finally, drying at very low relative humidity (< 25% RH) and/or at elevated temperature removes interlayer water between the silicate-rich C-S-H sheets of ≈ 2 nm spacing [19, 36, 38].

Drying not only increases the amount of accessible porosity, but also alters the pore structure. Dehydration of the Aft and AFm phases [39] and partial collapse of C-S-H sheets occur due to high surface energy or disjoining pressures [40], which in turn densifies the C-S-H and increases the size of capillary pores. Parrott et al. [41], using nitrogen adsorption, showed closure of small pores on first drying at 70-40% RH due to capillary tension stresses. Maruyama et al. [13] showed closure of gel pores in favour of creating larger capillary pores on drying particularly at < 50% RH. Recent ^{1}H NMR work [42] showed similar redistribution of pore structure in thin cement paste on first drying cycle, where large pores (> 20 nm) are created at the expense of collapsed gel pores (< 10 nm). Thus, drying causes the microstructure to undergo "coarsening" leading to more open pore structure.

Furthermore, macroscopic volume shrinkage occurs during drying and if restrained, induces stresses and surface microcracking when tensile strength is exceeded. Shrinkage is restrained by: a) internal material that dries at a slower rate than surface material, i.e. self-restraint, and b) stiff aggregate particles that shrink much less than the cement paste, i.e. aggregate-restraint. Samples dried at elevated temperatures experience steeper thermal and moisture gradients that contribute to more microcracking. These factors explain the characteristics of the observed interface/matrix cracks that propagate perpendicular to the drying surface, with their size, density and depth increasing with drying severity and aggregate size (Figs. 3-5). The observations are consistent with findings from other studies on drying-induced microcracking e.g. [3, 5-10].

All of the above changes may contribute to transport, but they can occur simultaneously and so are difficult to decouple. However, the gently step-wise dried samples at 21°C (Regime A) had the least microcracking and so the change in transport should mainly be related to emptying of pores. The latter can be deduced from the good correlation between transport properties and accessible porosity. But the gradual transport increase over the entire RH range (Figs. 9 & 10) suggests that there is not a particular pore type or size class that dominates the process. Rapid drying at 21°C (Regime B) and at elevated temperatures (Regimes C & D) caused further increase in transport relative to step-wise drying. This is because of the higher degree of microcracking (Fig. 4), greater proportion of water removed from C-S-H interlayer (Figs. 6 & 8) causing C-S-H collapse and coarsening of the pore structure.

4.2 Effects of rewetting and hysteresis

On rewetting, cementitious materials gain moisture via: a) adsorption that lines pore surfaces with increasing thickness of adsorbed water and this occurs over the entire RH range, and b) capillary condensation from about 40% RH to saturation, governed by thermodynamic equilibrium between liquid and vapour phase in pores. Therefore, the pore structure becomes increasingly filled and gaseous transport decreases. But the equilibrium moisture content at a particular RH is much lower on rewetting than on drying (Fig. 8), showing an apparent path (history) dependent behaviour.

Moisture hysteresis at high RH (> 50%) is usually attributed to two factors: a) complex random pore network consists of various pore sizes that are interconnected so small constrictions/necks prevent larger pore chambers from emptying at the equilibrium RH associated with their size, i.e. the "ink bottle" or "pore blocking" effect, and b) changes in the liquid-vapour curvature during wetting/drying means these processes occur at different RH. Hysteresis at low RH (<35%) is linked to the removal of interlayer water and C-S-H collapse [19, 20, 43-47], and this is partially irreversible on rewetting. Samples dried at elevated temperatures (Regimes C & D, Fig. 8) and then rewetted at 21°C showed larger hysteresis presumably due to greater loss of interlayer water and more severe collapse. Furthermore, there may be kinetic effects, i.e. delay in water re-entering collapsed pores that delays equilibrium and thus contributing to hysteresis [19, 42].

Swelling of the collapsed C-S-H occurs during rewetting and so drying shrinkage is partially recovered [41]. Filling of large capillary pores is difficult unless at very high RH, or if the sample is immersed in water or vacuum saturated [36]. Therefore, large pores remain empty or lined with a layer of adsorbed water until close to

100% RH. This is the same for microcracks, apart from locations of constrictions/necks where condensates may form first. On vacuum saturation, the water lost on first drying appears to be recovered (Fig. 8). In most cases, severely dried samples (Regimes C & D) gained a slightly larger amount of water on rewetting presumably due to filling of microcracks.

Very few studies have examined how moisture hysteresis influences mass transport, but our data (Figs. 10 & 11) clearly show this effect. Transport initially decreases modestly on rewetting due to the effects discussed earlier, but beyond ≈ 80% RH (Figs. 10 & 11) it rapidly drops to zero at near saturation. Throughout the whole RH range, samples have higher gaseous transport properties on rewetting than on drying. When plotted against degree of saturation (Figs. 12-14) however, the apparent hysteresis drastically reduces or disappears completely in some cases. The significant overlaps show that the discrepancies between transport measured on drying and rewetting are largely due to differences in moisture content, in agreement with moisture diffusivity results from sorption experiments [20, 27]. Therefore, plotting transport properties against degree of saturation takes account of sorption-desorption hysteresis. The strong correlations also show that saturation degree is a critical parameter controlling transport, which is not surprising since it is related to the fraction of empty porosity accessible to gas (Fig. 15).

4.3 Significance of drying-induced damage on transport

The most interesting finding is the "residual effect" of drying-induced damage (i.e. C-S-H collapse, pore coarsening and microcracking), i.e. the effect on transport once saturation degree has been accounted for. Oven dried samples (Regimes C & D) did show higher transport coefficients than gently dried samples (Regimes A & B) when rewetted to equal saturation degree, but the differences of ≈ 41% to 96% (i.e. up to factor of 2) for diffusivity and ≈ 54% to 354% (i.e. up to factor of 4) for permeability (Figs. 12-14) seem modest given the severity of drying and microcracking (Figs. 3 & 4). Surprisingly, drying-induced damage did not greatly increase rewetting rates (Table 4) nor electrical conductivity (< 53%) after vacuum saturation (Fig. 16a). Again, we observe that permeability is most sensitive to damage as was reported in previous studies [9, 12, 33, 48].

It is worthwhile to compare the findings above to other studies. Wu et al. [11] measured gas permeability of microcracked concrete (50°C and 105°C dried) at confining pressures from 0.3 to 1.9 MPa. Here moisture content was constant so its effect was essentially isolated. They showed that increasing confinement caused partial closure of microcracks and permeability decreased by up to 46%. Similarly, Mills [49] and Lion et al. [50] observed gas permeability decreased by up to 50% when measured at increasing confinement pressure to ≈28 MPa. They suspected microcrack closure, but did not provide supporting evidence. Dehghanpoor Abyaneh et al. [48] simulated concrete containing microcracks using a three-dimensional mesoscale model. They carried out a sensitivity analysis of the effect of bond and matrix microcracks of varying widths (1-50μm), crack pattern, vol. fraction and percolation degree. The simulations showed that concretes with less than 1% vol. microcracks that are sparsely distributed and non-percolated could increase diffusivity by ≈100% and permeability by ≈400%. Bisschop and van Mier [51] found little influence of microcracks on the drying rates. These seem broadly in line with our findings.

Several factors could mitigate the impact of drying-induced damage when samples are rewetted. These include blockage by capillary condensation at narrow crack constrictions, swelling of the C-S-H at the expense of capillary porosity and continued hydration of exposed unreacted binders causing crack healing [5, 52-54] and reduction in capillary porosity. The effect of further hydration should be more noticeable on the young (3 days) samples and at high RHs. Therefore, microcracks partially close on rewetting and the slow nature of the conditioning regime (Fig. 6) exacerbates some of these effects. Microcracking was found in all samples and increased with drying severity, but contributed only a small fraction of the total accessible porosity (Fig. 16b). Our earlier study [12] presented a more comprehensive image analysis of microcracks and found that the microcracks contributed only 0.1-1.3% of total porosity. Furthermore, microcracks do not propagate through the entire sample thickness, but are concentrated near the exposed surface to depths of several mm (Fig. 3).

A pertinent study showing the effects of rewetting is that of Hearn [24] who compared the permeability of mortars to water and propan-2-ol. The mortars were dried at 105°C, then resaturated with either water or propan-2-ol and retested. She observed that the water permeability of oven-dried and resaturated mortar was initially

higher (up to a factor of 2) but this decreased back to the level of the virgin (never dried) mortar when the test continued for 100 h. This behaviour was attributed to C-S-H swelling on resaturation, self-healing of cracks and possibly dissolution and re-deposition of hydrates during water permeability testing. In contrast, propan-2-ol permeability of oven-dried and resaturated mortar was higher (up to an order of magnitude) than the virgin mortar and this remained constant during prolonged testing. This is because propan-2-ol has no chemical or physical interaction with the sample, therefore the C-S-H remains in a state of collapse, there is an absence of self-healing and the drying-induced cracks are able to increase flow substantially.

4.4 Supplementary cementitious materials

At all conditioning stages, samples with SCMs showed lower drying rates (Table 4), therefore higher water contents (Fig. 6) and saturation degrees (Fig. 7), and lower gaseous transport properties (Figs. 2, 10 & 11) compared to equivalent samples containing CEM I only. Even when comparison was made at equal saturation degree, samples containing SCMs consistently gave lower transport properties (Fig. 14). Saturated electrical conductivity was also significantly lower (Fig. 16a). SF gave marginally better results than GGBS. The beneficial effect of SCMs on mass transport properties is well-established, see for example [55, 56]. Nevertheless, total porosity was not much affected (Fig. 16b). All of these are consistent with the fact that the presence of SCMs changes the type and amount of hydrates formed in particular the C-S-H [57]. This increases the internal surface area and refines the pore structure relative to CEM I systems. However, the water within gel pores and C-S-H is removable on severe drying at elevated temperature (Fig. 6 g, h) and this explains the large percentage increase in gaseous transport for samples containing SCMs (Fig. 2 b, d). Therefore, concretes containing SCMs are more sensitive to severe drying. Furthermore, the effect of drying induced damage is more pronounced for systems with denser matrix in agreement with 3D simulations [48].

4.5 Implications

It is pertinent to explore the relevance of this study to practice. Real concrete structures experience more internal restraint from the bulk concrete, as well as external restraint from adjacent members and formwork and load induced stresses. These may cause large “macro” cracking (> 0.1 mm), the effects of which are not included here. However, these should be controlled by appropriate structural design and judicious use and placement of steel reinforcement. Real concrete structures are subjected to daily fluctuations in humidity and temperature in natural environments, but these are normally within a much narrower range than those applied here. Furthermore, the changes occur over shorter time intervals, so real concrete structures generally experience less extreme moisture/temperature gradients and less complete drying compared to those imposed in this study. This is beneficial for systems containing SCMs, where the lower drying rates and better moisture retention means such systems will have greater resistance to transport and degradation. One exception is structures exposed to a dry environment where carbonation is the main degradation process.

In addition, external drying in real concrete structures occurs mainly through one exposed surface. Asymmetric suction in pores causes warping (concave toward drying surface) [58], the resultant bending stresses reduce tension at the surface and thereby crack density. In this study however, drying was allowed to occur on both opposite sides of the sample and this should induce more severe microcracking. Therefore, the samples tested in this study are subjected to more extreme conditions and are likely to be more microcracked than in real concrete structures. In this respect, the amount of drying-induced damage and the observed effects represent a worst-case scenario in relation to most practical situations.

Real concrete structures are also exposed to cyclic drying-wetting. We were unable to test beyond one drying and rewetting cycle due to time limitations and the slow nature of the conditioning regimes. However, it is fairly well-established that most of the changes to microstructure occur on first drying and subsequent drying cycles impose little, if any further changes [36]. Drying shrinkage is also largest during the first drying cycle, the strains developed in subsequent cycles are nearly elastic and reversible [14]. However, a prolong wetting period will enhance hydration and healing as discussed earlier. Therefore, it may be speculated that the observed residual effects in this study are on the conservative side and that subsequent cycles will be no greater than this.

5. Conclusions

Mass transport and microstructural properties of a range of pastes, mortars and concretes were tested after being subjected to several drying and rewetting regimes (by humidification and full saturation) over a period of three years. Variables included w/b ratio (0.35 and 0.50), binder type (CEM I, CEM I with 10% silica fume replacement, and CEM III containing 70% GGBS), aggregate size (5 and 10 mm), curing age (3 and 90 days) and conditioning regimes. Oxygen diffusivity and permeability, electrical conductivity, porosity and degree of microcracking were examined. The study was an attempt to isolate the effects of drying-induced damage and moisture content on mass transport, and to understand the influence of rewetting on the transport properties of micro-cracked cementitious materials. The overall aim was to better understand the effects of shrinkage, moisture hysteresis and drying-induced microcracking on long-term durability of concrete.

The main findings are as follows:

a) Drying induces a greater change in transport properties compared to varying w/b ratios, curing ages or SCMs. Stepwise drying at 21°C: 93% RH → 3% RH can increase gaseous transport by an order of magnitude while drying at 105°C increases it by nearly two orders of magnitude. This is due to a combination of factors: emptying of pores (capillaries, gels, interlayer) increasing porosity accessible to gas, changes to microstructure (C-S-H collapse, pore coarsening) and shrinkage induced microcracking.

b) Drying induces surface microcracking of widths ≈1 to 60 μm with map-cracking that propagates approximately perpendicular into the sample to depths of several mm (< 10 mm). The width, length, density and penetration depth of microcracks increase with severity of drying. Microcracking also increases with increase in w/b ratio and aggregate particle size.

c) Significant moisture and transport hysteresis occur over a wide RH range when dried samples are rewetted. However, the apparent hysteresis decreases substantially when the data are plotted against degree of saturation. Thus, the discrepancies between transport measured on drying and rewetting are largely due to differences in moisture content, which is related to the fraction of empty porosity accessible to gas. Plotting transport properties against degree of saturation takes account of sorption-desorption hysteresis.

d) Severely dried samples (50°C and 105°C) show higher gaseous transport properties than gently step-wise dried samples (21°C) when they are rewetted and compared at equal saturation degree. The largest differences range from 41% to 96% for diffusivity, and 54% to 354% for permeability. These represent the maximum residual effects of drying on transport after accounting for moisture content. Drying-induced damage did not greatly increase rewetting rates, total porosity or electrical conductivity after vacuum saturation. The impact of cracks is probably mitigated by blockage via moisture condensation at narrow constrictions, swelling of the C-S-H and further hydration of exposed unreacted cement causing self-healing.

e) At all conditioning stages, samples containing SCMs (GGBS and SF) showed lower drying rates, therefore higher water contents and saturation degrees, and lower gaseous transport properties compared to equivalent samples with CEM I only. Even when compared at equal saturation degree, samples containing SCMs consistently gave lower transport properties. At saturation, electrical conductivity was also significantly lower, but total porosity was not greatly affected. SF performed marginally better than GGBS. These are consistent with the fact that SCMs changes the type and amount of hydrates formed, in particular the C-S-H, increasing internal surface area and refining pore structure relative to CEM I.

f) The amount of water retained after equilibrium at a particular RH is approximately the same for pastes, mortars and concretes of the same binder type, w/b ratio and curing age, if moisture content is expressed as a fraction of cement content. Thus, aggregate particles and the aggregate-paste "interfacial-transition zone" (ITZ) do not influence equilibrium moisture content or moisture transport properties.

g) Real concrete structures in common exposure environments (except for carbonation in a dry environment) are exposed to less extreme moisture or temperature gradients, shorter drying-wetting cycles and less complete drying to those imposed in this study. Therefore, real concrete structures are likely to be less

micro-cracked than the samples tested in this study. On this basis, one may conclude that drying-induced microcracks would have little impact on the durability of common concrete structures in the field.

6. Acknowledgments

We would like to acknowledge the funding from the UK-China Scholarships for Excellence programme, provided by the UK Department for Business Innovation & Skills and the China Scholarship Council. We also thank Mr. Andrew Morris for his help with the laboratory work.

References

[1] F.O. Slate, S. Olsefski (1963) X-rays for study of internal structure and microcracking of concrete. J Am Concr Inst 60:575–588

[2] H.R. Samaha, K. Hover (1992) Influence of microcracking on the mass transport properties of concrete. ACI Mater J 89: 416–424

[3] C. L. Hwang, J. F. Young (1984), Drying shrinkage of Portland cement pastes I. Microcracking during drying, Cem. Concr. Res., 14, 585-594.

[4] Z.P. Bazant, S. Sener, J.K. Kim (1987), Effect of cracking on drying permeability and diffusivity of concrete. ACI Mater. J., 84, 351–357.

[5] K. O. Kjellsen, H. M. Jennings (1996), Observations of microcracking in cement paste upon drying and rewetting by environmental scanning electron microscopy, Advanced Cement Based Materials, 3, 14-19.

[6] J. Bisschop, J.G.M. van Mier (2002), Effect of aggregates on drying shrinkage microcracking in cement-based composites, Mater. Struc., 35, 453–461.

[7] J. Bisschop, F.K. Wittel (2011), Contraction gradient induced microcracking in hardened cement paste. Cem. Concr. Compos. 33, 466–473.

[8] A. Idiart, J. Bisschop, A. Caballero, P. Lura (2012), A numerical and experimental study of aggregate-induced shrinkage cracking in cementitious composites. Cem. Concr. Res., 42, 272–281

[9] H. S. Wong, N. R. Buenfeld, J. Hill, A.W. Harris (2007), Mass transport properties of mature wasteform grouts, Advances in Cement Research, 19, 35-46.

[10] I. Maruyama, H. Sasano (2014), Strain and crack distribution in concrete during drying, Mater. Struct. 47, 517-532.

[11] Z. Wu, H.S. Wong, N.R. Buenfeld (2014), Effect of confining pressure and microcracks on mass transport properties of concrete, Advances in Applied Ceramics, 113, 485-495.

[12] Z. Wu, H.S. Wong, N.R. Buenfeld (2015), Influence of drying-induced microcracking and related size effects on mass transport properties of concrete, Cem. Concr. Res., 68, 35-48.

[13] I. Maruyama, Y. Nishioka, G. Igarashi, K. Matsui (2014), Microstructural and bulk property changes in hardened cement paste during the first drying process, Cem. Concr. Res. 58 (2014) 20–34.

[14] G. W. Scherer (2015), Drying, shrinkage and cracking of cementitious materials, Transport in Porous Media, 1-21.

[15] Y.F. Houst, F.H. Wittmann (1994), Influence of porosity and water content on the diffusivity of CO_2 and O_2 through hydrated cement paste, Cem. Concr. Res., 24 (6) 1165-1176.

[16] A. Abbas, M. Carcasses, J.P. Ollivier (1999), Gas permeability of concrete in relation to its degree of saturation, Mater. Struct. 32 (1) 3-8.

[17] L.O. Nilsson (2002), Long-term moisture transport in high performance concrete, Mater. Struct. 35 (10) 641-649.

[18] J. Sercombe, R. Vidal, C. Gallé, F. Adenot (2007), Experimental study of gas diffusion in cement paste, Cem. Concr. Res., 37, 579-588.

[19] V. Baroghel-Bouny (2007), Water vapour sorption experiments on hardened cementitious materials. Part I: Essential tool for analysis of hygral behaviour and its relation to pore structure, Cem. Concr. Res., 37, 414-437.

[20] V. Baroghel-Bouny (2007), Water vapour sorption experiments on hardened cementitious materials. Part II: Essential tool for assessment of transport properties and for durability, Cem. Concr. Res., 37, 438-454.

[21] Z. Zhang, M. Thiéry, V. Baroghel-Bouny (2014), A review and statistical study of existing hysteresis models for cementitious materials, Cement and Concrete Research, 57, 44-60.

[22] Concrete Society (2010), Technical Report 22: Non-structural cracks in concrete, 4th Edition, Camberley.

[23] T. C. Powers, L. E. Copeland, J. C. Hayes, H. M. Mann (1955), Permeability of Portland cement paste, Bull. Portland Cem. Assoc. 53, 285–298

[24] N. Hearn (1996), Comparison of water and propan-2-ol permeability in mortar specimens, Adv. Cem. Res. 8 (30) 81–86 (1996).

[25] N. Hearn (1999), Effect of shrinkage and load-induced cracking on water permeability of concrete, ACI Mat. J., 96, 234-241.

[26] M. Saiedpour, L. Wadső (2016), Moisture diffusion coefficients of mortars in absorption and desorption, Cem. Concr. Res., 83, 179-187.

[27] M. Saiedpour, L. Wadső (2016), The influence of sorption hysteresis on diffusion coefficients represented with different moisture potentials, Cem. Concr. Res., 90, 1-5.

[28] Z.P. Bazant, W.J. Raftshol (1982), Effect of cracking in drying and shrinkage specimens, Cem. Concr. Res. 12, 209–226.

[29] H.S. Wong, K. Matter, N.R. Buenfeld (2013), Estimating the original cement content and water-cement ratio (w/c) of Portland cement concrete and mortar using backscattered electron microscopy, Mag. Concr. Res., 65 (11) 693-706.

[30] F.E.M. O'Brien (1948), The control of humidity by saturated salt solutions, J. Sci. Instrum., 25, 73-76.

[31] A. Wexler, S. Hasegawa (1954), Relative humidity-temperature relationships of some saturated salt solutions in the temperature range 0°C to 50°C, Journal of Research of the National Bureau of Standards, 53 (1) 19-26.

[32] RILEM TC 116-PCD (1999), Permeability of concrete as a criterion of its durability, Mater. Struct., 32, 174-179.

[33] H.S. Wong, M. Zobel, N.R. Buenfeld, R.W. Zimmerman (2009), Influence of the interfacial transition zone and microcracking on the diffusivity, permeability and sorptivity of cement-based materials after drying, Mag. Concr. Res., 61 [8] 571-589.

[34] S. Dehghanpoor Abyaneh, H.S. Wong, N.R. Buenfeld (2013), Modelling the diffusivity of mortar and concrete using a three-dimensional mesostructure with several aggregate shapes, Computational Materials Science, 78, 63-73.

[35] H.S. Wong, R.W. Zimmerman, N.R. Buenfeld (2012), Estimating the permeability of cement pastes and mortars using image analysis and effective medium theory, Cem. Concr. Res., 42, 476-483.

[36] H.M. Jennings, A. Kumar, G. Sant (2015), Quantitative discrimination of the nano-pore structure of cement paste during drying: new insights from water sorption isotherms, Cem. Concr. Res. 76, 26–36,

[37] A.C.A. Muller, K.L. Scrivener, A.M. Gajewicz, P.J. McDonald (2013), Use of bench-top NMR to measure the density, composition and desorption isotherm of C-S-H in cement paste, Microporous Mesoporous Mater., 178, 99–103.

[38] H.M. Jennings (2008), Refinements to colloid model of C-S-H in cement: CM-II, Cem. Concr Res. 38, 275–289,

[39] L. Zhang, F.P. Glasser (2000), Critical examination of drying damage to cement pastes, Advances in Cement Research, 12, 79-88.

[40] F. Beltzung, F.H. Wittmann (2005), Role of disjoining pressure in cement based materials. Cem. Concr. Res. 35, 2364–2370.

[41] L.J. Parrott, W. Hansen, R.L. Berger (1980), Effect of first drying upon the pore structure of hydrated alite paste, Cem. Concr. Res. 10, 647–655.

[42] A.M. Gajewicz, E. Gartner, K. Kang, P.J. McDonald, V. Yermakou (2016), A ^{1}H NMR relaxometry investigation of gel-pore drying shrinkage in cement pastes, Cem. Concr. Res. 86, 12–19.

[43] R.F. Feldman (1968), Sorption and length change scanning isotherms of methanol and water on hydrated Portland cement paste, Proc. Of 5th Internatioanl Congress on the Chemistry of Cement, Vol 3, Tokyo, 53-66.

[44] R.F. Feldman, P.J. Sereda (1968), A model for hydrated Portland cement paste as deduced from sorption-length change and mechanical properties, Matériaux et Construction, 1 (6) 509-520.

[45] R.M. Espinosa, L. Franke (2006), Influence of the age and drying process on pore structure and sorption isotherms of hardened cement paste, Cem. Concr. Res., 36 (10) 1969-1984.

[46] R.M. Espinosa, L. Franke (2006b), Inkbottle pore-method: Prediction of hygroscopic water content in hardened cement paste at variable climatic condition, Cem. Concr. Res., 36 (10) 1969-1984.

[47] J.J. Thomas, A.J. Allen, H.M. Jennings (2008), Structural changes to the calcium-silicate-hydrate gel phase of hydrated cement with age, drying and resaturation, J. Amer. Ceram. Soc., 91 (10) 3362-3369.

[48] S. Dehghanpoor Abyaneh, H.S. Wong, N.R. Buenfeld (2016), Simulating the effect of microcracks on the diffusivity and permeability of concrete using a three-dimensional model, Computational Materials Science, 119, 130-143

[49] R. H. Mills (1987), Mass transfer of gas and water through concrete, American Concrete Institute SP-100, 621-644.

[50] M. Lion, F. Skoczylas, Z. Lafhaj, M. Sersar (2005), Experimental study on a mortar. Temperature effects on porosity and permeability. Residual properties or direct measurements under temperature, Cem. Concr. Res., 35, 1937-1942.

[51] Bisschop, J., van Mier, J.G.M.(2008), Effect of aggregates and microcracks on the drying rate of cementitious composites. Cem. Concr. Res. 38, 1190–1196.

[52] N. Hearn (1998), Self-sealing, autogenous healing and continued hydration: What is the difference? Mater. Struct., 31, 563-567

[53] C. Edvardsen (1999), Water permeability and autogenous healing of cracks in concrete, ACI Mater. J., 96, 4, 448-454

[54] H-W. Reinhardt, M. Joss (2003), Permeability and self-healing of cracked concrete as a function of temperature and crack width, Cem. Concr. Res., 33, 981-985.

[55] E.J. Sellevold, T. Nilsen (1987), Condensed silica fume in concrete: A world review, in: Supplementary Cementing Materials for Concrete, V.M. Mahotra (eds.), CANMET, Ottawa, 165-243.

[56] R.D. Hooton (1986), Permeability and pore structure of cement pastes containing fly ash, slag, and silica fume, Blended Cements, ASTM STP 897, G. Frohnsdorff (eds.), American Society for Testing and Materials, Philadelphia, pp.128-143.

[57] B. Lothenbach, K.L. Scrivener, R.D. Hooton (2011), Supplementary cementitious materials, Cem. Concr. Res., 41, 1244-1256.

[58] G.W. Scherer (1987), Drying gels: III. Warping plate. J. Non-Cryst. Solids, 91, 83–100

Table 1 Oxide composition and loss on ignition of the binders used.

Binder	Oxide composition (%)									Loss on ignition (%)
	CaO	SiO_2	Al_2O_3	Fe_2O_3	MgO	Na_2O	K_2O	SO_3	Cl-	
CEM I, 32.5R	63.4	20.6	5.6	2.4	1.6	0.2	0.7	2.9	< 0.1	2.1
CEM III / B 42.5N (contains 70% GGBS)	48.0	29.2	8.9	1.2	4.8	0.2	0.6	2.6	< 0.1	1.4
Silica fume	0.15	98.70	0.31	0.02	0.04	0.09	0.30	-	-	0.47

Table 2 Mix proportions.

Mix	Binder: kg/m^3			Water: kg/m^3	Free w/b	Limestone: kg/m^3	Sand: kg/m^3	Agg. vol fraction: %
	CEM I	CEM III	SF					
C 0.5	374.9	-	-	194.2	0.50	1077.3	718.2	68
C 0.35	458.0	-	-	160.3	0.35	1077.3	718.2	68
C-SF 0.35	396.4	-	44.0	166.0	0.35	1077.3	718.2	68
C-SG 0.35	-	431.2	-	166.0	0.35	1077.3	718.2	68
M 0.5	471.7	-	-	240.6	0.50	-	1524.0	60
M 0.35	724.0	-	-	257.3	0.35	-	1270.0	50
P 0.5	1197.4	-	-	598.7	0.50	-	-	-
P 0.35	1462.8	-	-	512.0	0.35	-	-	-

Note: C = concrete; M = mortar; P = paste; SF = silica fume; SG = slag.

Table 3 Total length and density of microcracks measured on surface exposed to drying.

Sample	21°C, 55% RH (stepwise)			21°C, 33%RH			50°C, 7% RH			105°C		
	Image area (mm^2)	Length (mm)	Density (mm^{-1})	Image area (mm^2)	Length (mm)	Density (mm^{-1})	Image area (mm^2)	Length (mm)	Density (mm^{-1})	Image area (mm^2)	Length (mm)	Density (mm^{-1})
P 0.35-3d	3690	6.1	0.002	3771	105.1	0.028	3603	203.7	0.057	3813	563.3	0.148
P 0.5-3d	3772	12.5	0.003	3792	626.2	0.165	3801	686.1	0.181	3801	1500.9	0.395
C 0.5-3d	192	16.9	0.088	192	19.8	0.103	192	43.2	0.225	192	92.5	0.482

Table 4 Average desorption and sorption coefficients (% / day$^{0.5}$) for conditioning regimes (A, B, C, D). Numbers in brackets are standard errors.

Mix	Curing age (d)	Desorption (% / day$^{0.5}$)				Sorption (% / day$^{0.5}$)			
		A	B	C	D	A	B	C	D
P 0.5	3	- 0.400 (0.006)	- 1.56 (0.009)	- 4.25 (0.015)	- 14.6 (0.131)	-	0.245 (0.002)	0.351 (0.002)	0.248 (0.001)
	90	- 0.294 (0.005)	- 0.447 (0.001)	- 1.69 (0.004)	- 6.07 (0.031)	-	0.339 (0.005)	0.313 (0.003)	0.310 (0.002)
P 0.35	3	- 0.347 (0.005)	- 0.616 (0.003)	- 2.26 (0.122)	- 8.50 (0.058)	-	0.226 (0.007)	0.311 (0.001)	0.285 (0.014)
	90	- 0.247 (0.002)	- 0.435 (0.004)	- 1.83 (0.001)	- 7.29 (0.076)	-	0.264 (0.002)	0.359 (0.004)	0.339 (0.001)
M 0.5	3	- 0.180 (0.003)	- 0.449 (0.008)	- 1.12 (0.024)	- 5.11 (0.032)	-	0.085 (0.006)	0.088 (0.001)	0.075 (0.003)
	90	- 0.138 (0.008)	- 0.146 (0.005)	- 0.656 (0.012)	- 3.97 (0.063)	-	0.121 (0.002)	0.119 (0.001)	0.132 (0.001)
M 0.35	3	- 0.174 (0.002)	- 0.293 (0.003)	- 1.09 (0.014)	- 3.99 (0.068)	-	0.102 (0.002)	0.093 (0.001)	0.094 (0.002)
	90	- 0.179 (0.002)	- 0.152 (0.002)	- 0.689 (0.014)	- 2.37 (0.101)	-	0.040 (0.001)	0.135 (0.001)	0.155 (0.002)
C 0.5	3	- 0.128 (0.002)	- 0.351 (0.012)	- 0.836 (0.019)	- 2.53 (0.039)	-	0.055 (0.003)	0.079 (0.001)	0.051 (0.001)
	90	- 0.118 (0.001)	- 0.122 (0.003)	- 0.452 (0.017)	- 0.871 (0.055)	-	0.063 (0.003)	0.067 (0.001)	0.095 (0.003)
C 0.35	3	- 0.101 (0.002)	- 0.196 (0.003)	- 0.625 (0.010)	- 2.11 (0.021)	-	0.050 (0.019)	0.083 (0.001)	0.058 (0.004)
	90	- 0.084 (0.003)	- 0.106 (0.002)	- 0.393 (0.007)	- 1.17 (0.014)	-	0.078 (0.003)	0.081 (0.003)	0.084 (0.001)
C-SF 0.35	90	- 0.033 (0.001)	- 0.059 (0.001)	- 0.308 (0.001)	- 1.74 (0.014)	-	0.026 (0.001)	0.098 (0.001)	0.092 (0.002)
C-SG 0.35	90	- 0.070 (0.002)	- 0.082 (0.004)	- 0.327 (0.020)	- 1.89 (0.053)	-	0.037 (0.002)	0.088 (0.003)	0.093 (0.004)

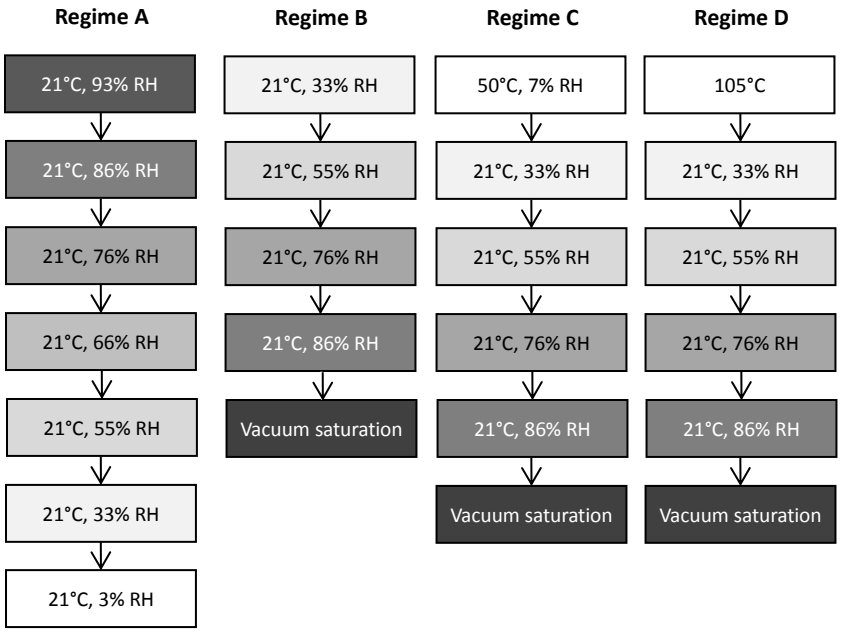

Figure 1 Summary of four conditioning regimes (A, B, C, D) applied. Each consists of drying and rewetting stages as shown. Transport measurements were carried out when samples achieved mass equilibrium at every stage.

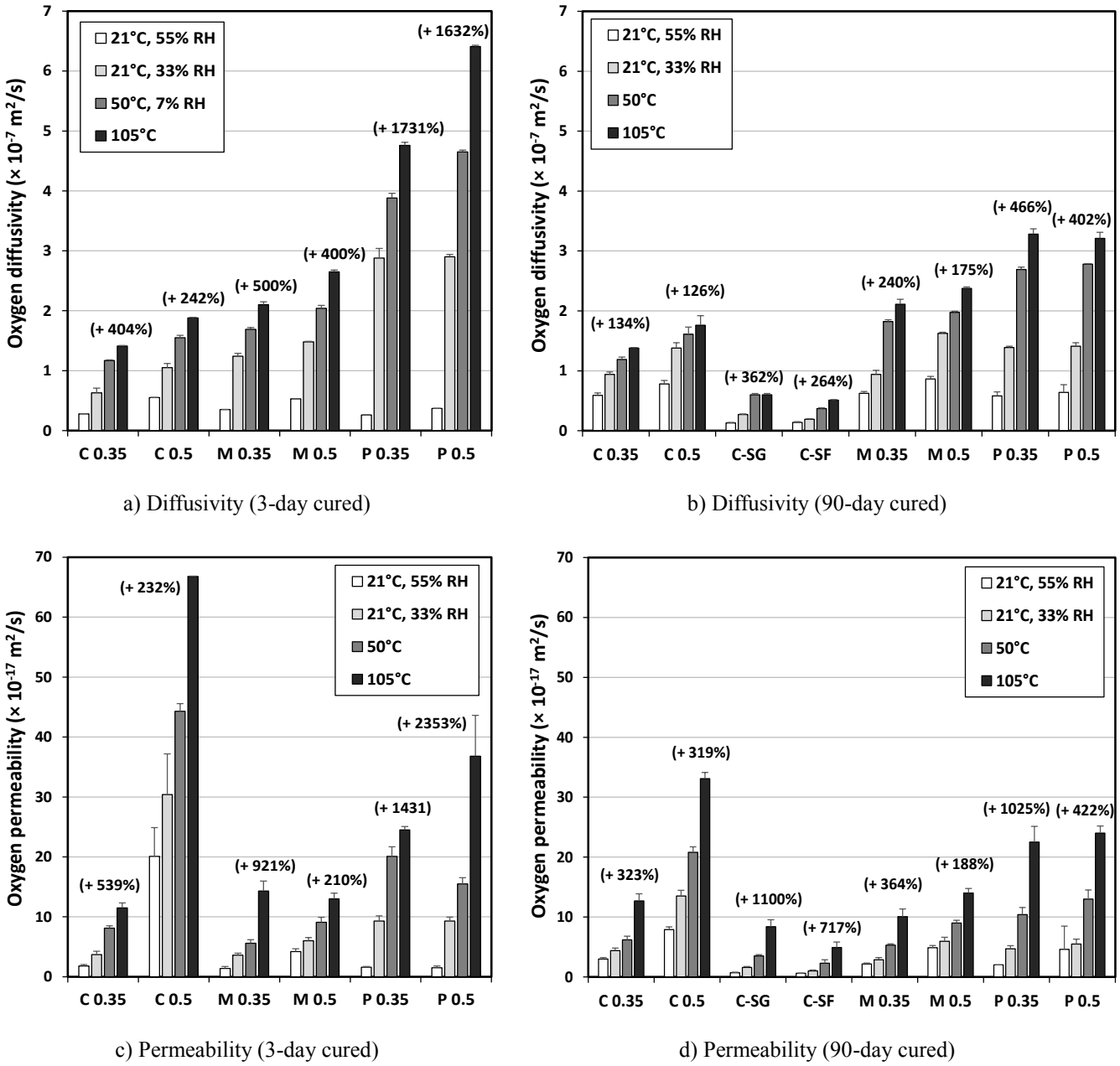

Figure 2 Oxygen diffusivity and permeability of selected concrete, mortar and paste samples after drying at 21ºC / 55% RH (stepwise), 21ºC / 33% RH, 50ºC and 105ºC. Numbers in brackets represent percentage increase at 105°C relative to 21°C / 55% RH.

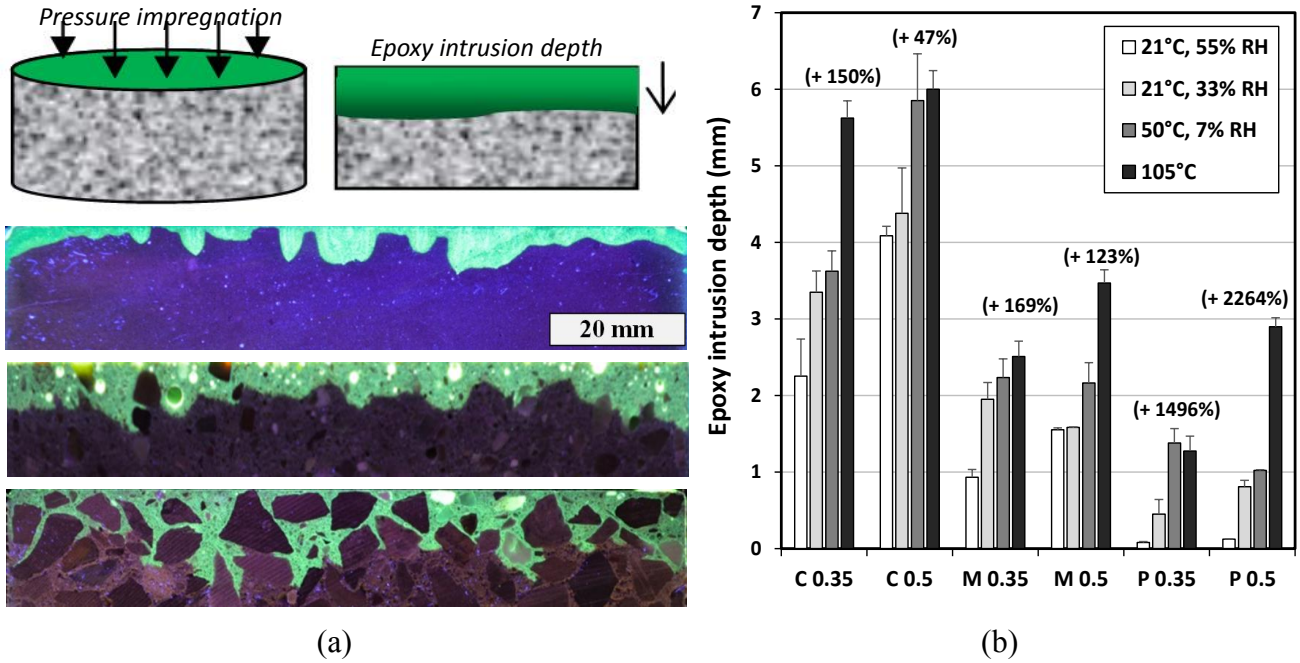

Figure 3 a) Cross-sections of paste, mortar and concrete samples showing depth of epoxy intrusion, and b) average epoxy intrusion depth of samples after drying at 21ºC / 55% RH (stepwise), 21ºC / 33% RH, 50ºC and 105ºC.

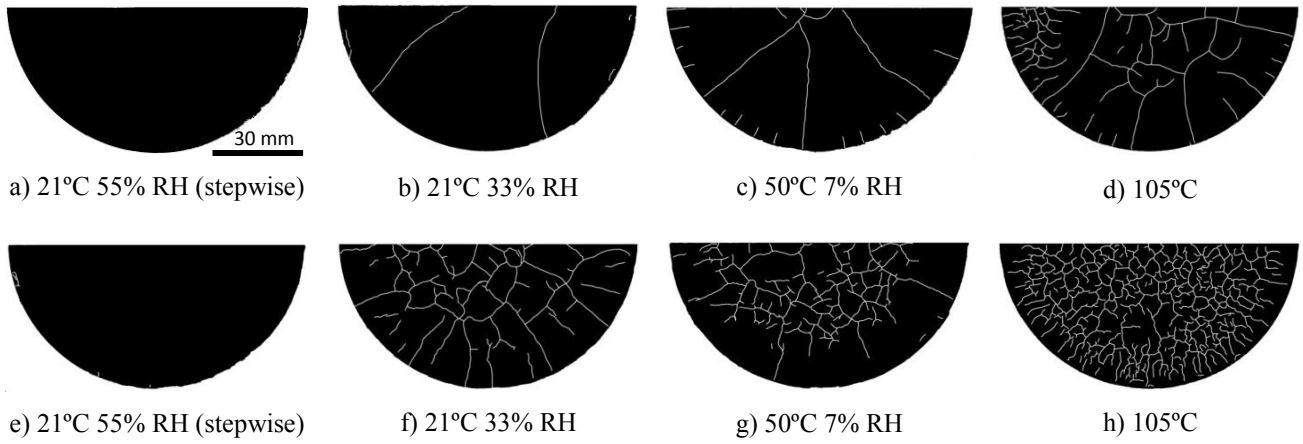

Figure 4 Effect of drying on surface microcracking of 3-day cured pastes of w/c 0.35 (a to d) and w/c 0.50 (e to h).

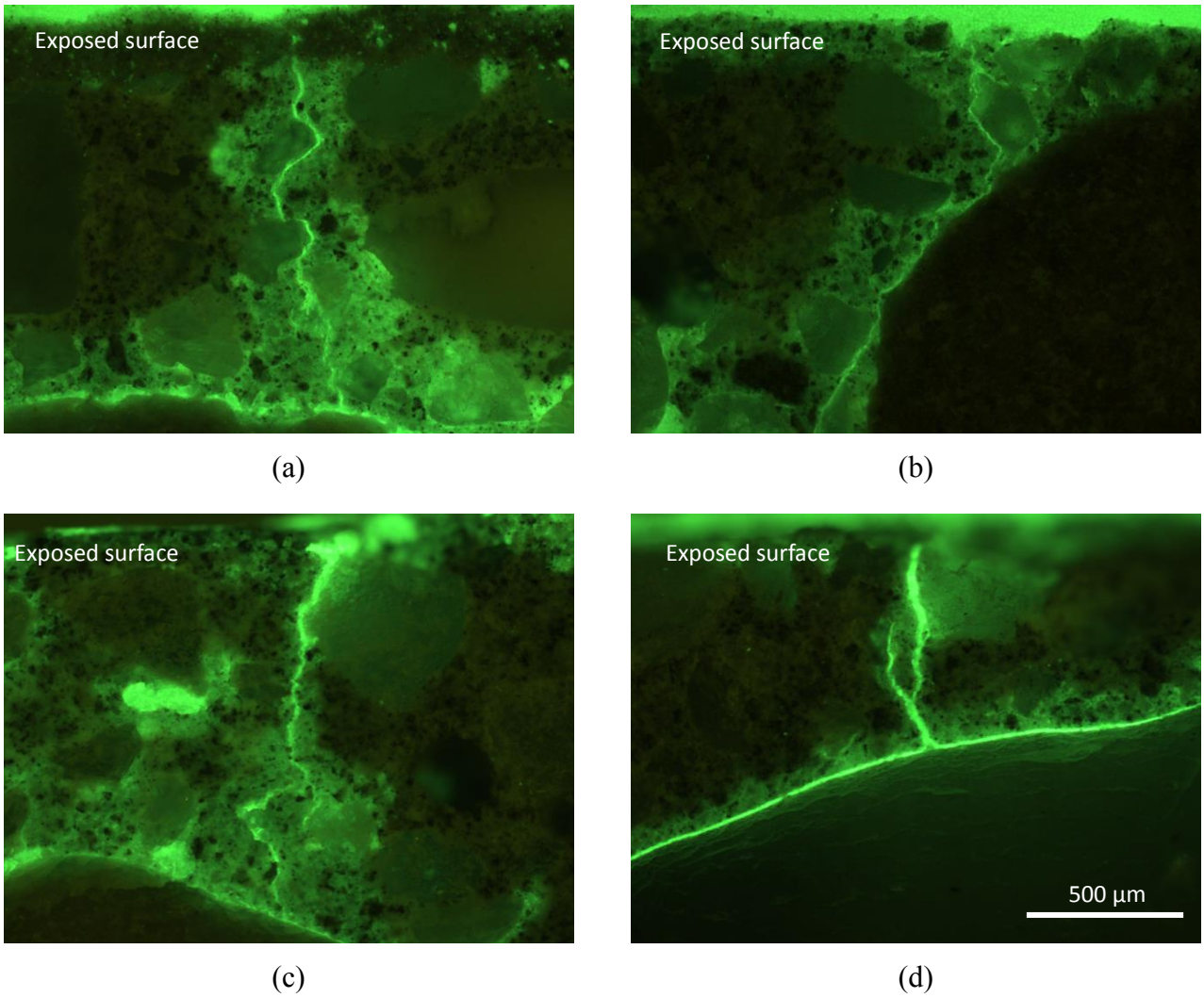

Figure 5 Fluorescence microscopy images showing example microcracks on cross-sections of concrete samples after drying at 21ºC, 33% RH. The microcracks are typically 1-60 µm wide propagating vertically from the exposed drying surface (top). Samples are C 0.5 (a, b) and C 0.35 (c, d). Field of view: 1820 × 1370 µm.

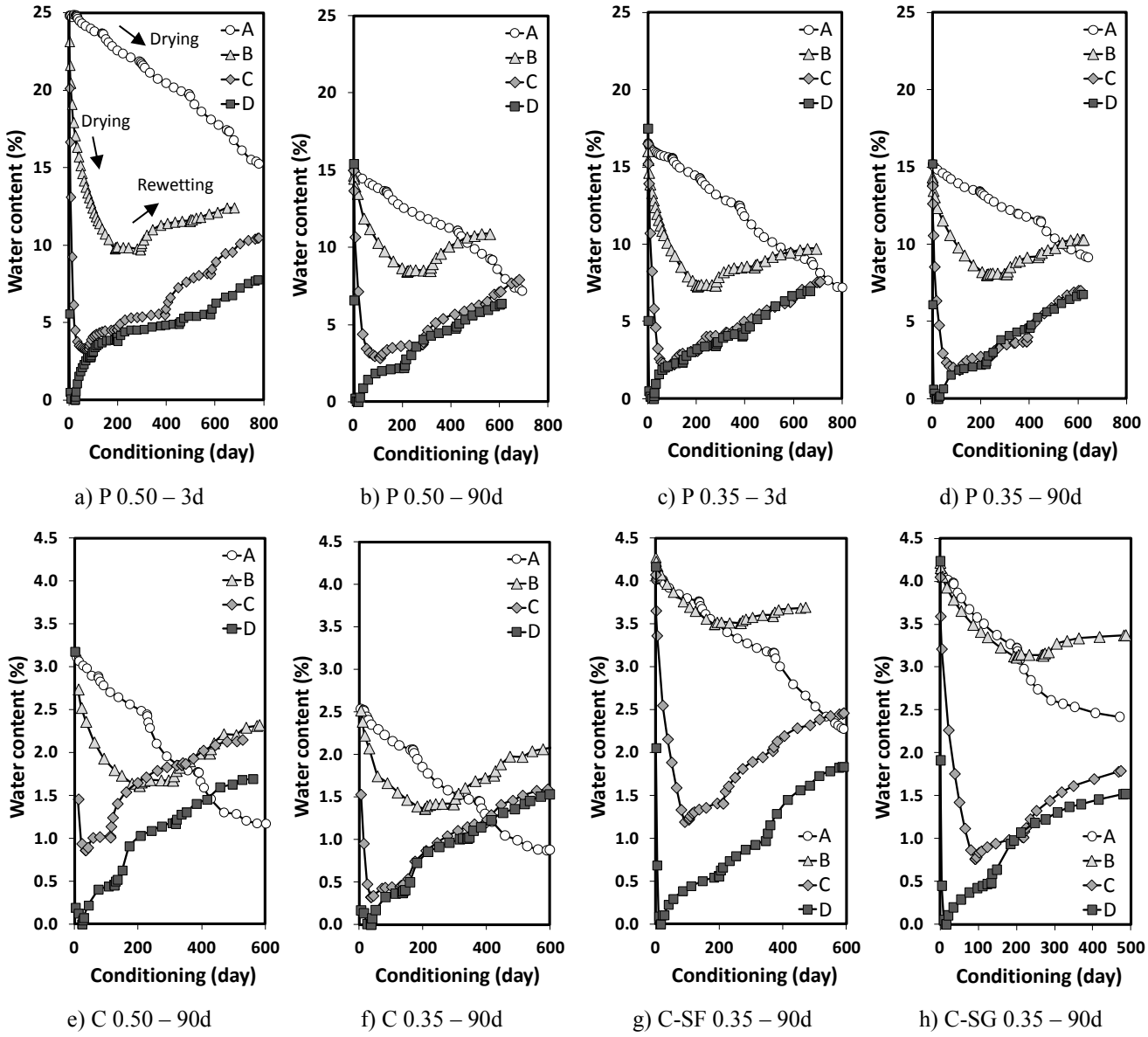

Figure 6 Evolution of moisture content for pastes and concretes with different binder types, w/b ratios and curing ages when subjected to conditioning regimes shown in Fig. 1.

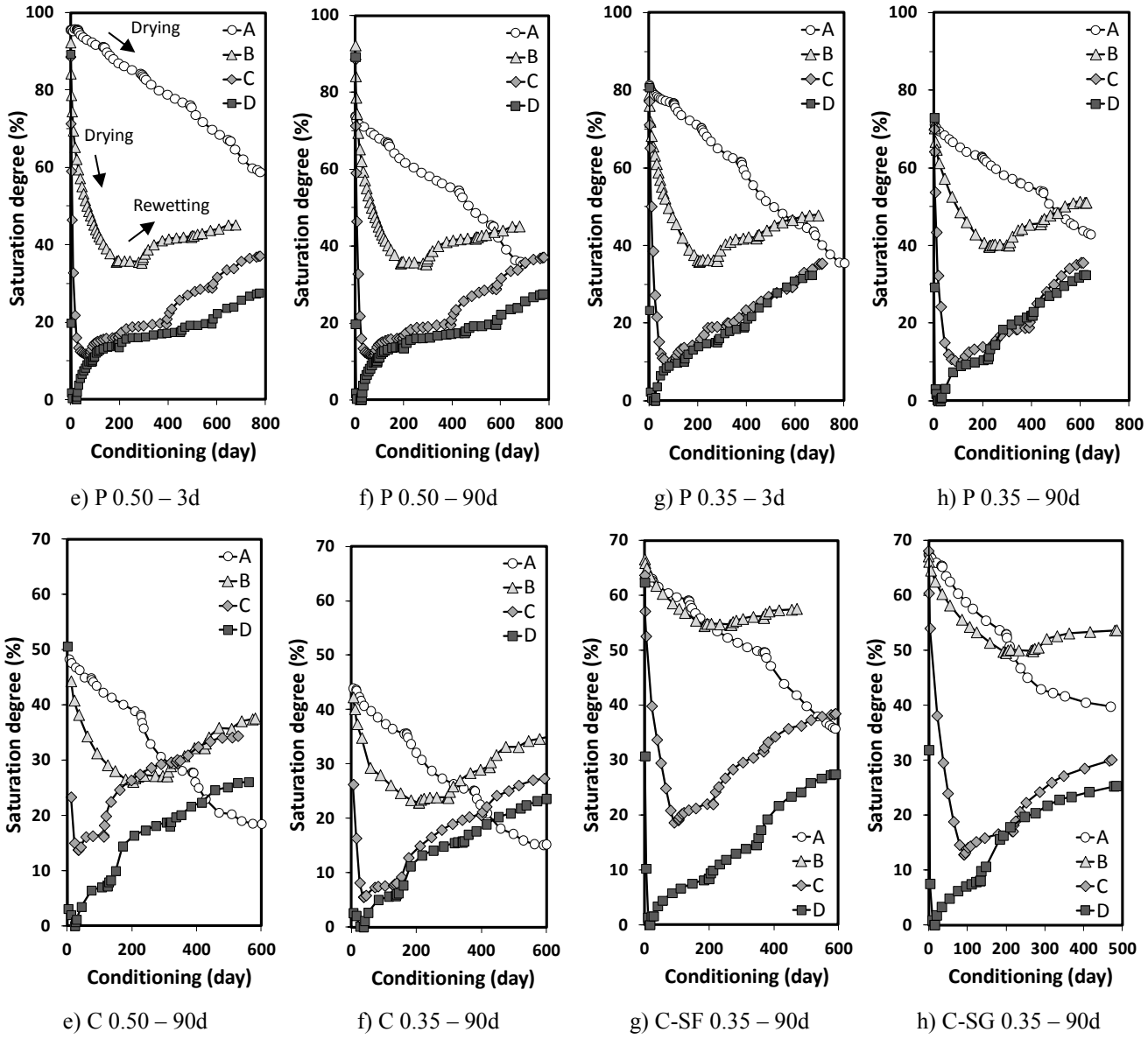

e) P 0.50 – 3d f) P 0.50 – 90d g) P 0.35 – 3d h) P 0.35 – 90d

e) C 0.50 – 90d f) C 0.35 – 90d g) C-SF 0.35 – 90d h) C-SG 0.35 – 90d

Figure 7 Evolution of saturation degree for pastes and concretes with different binder types, w/b ratios and curing ages when subjected to conditioning regimes shown in Fig. 1.

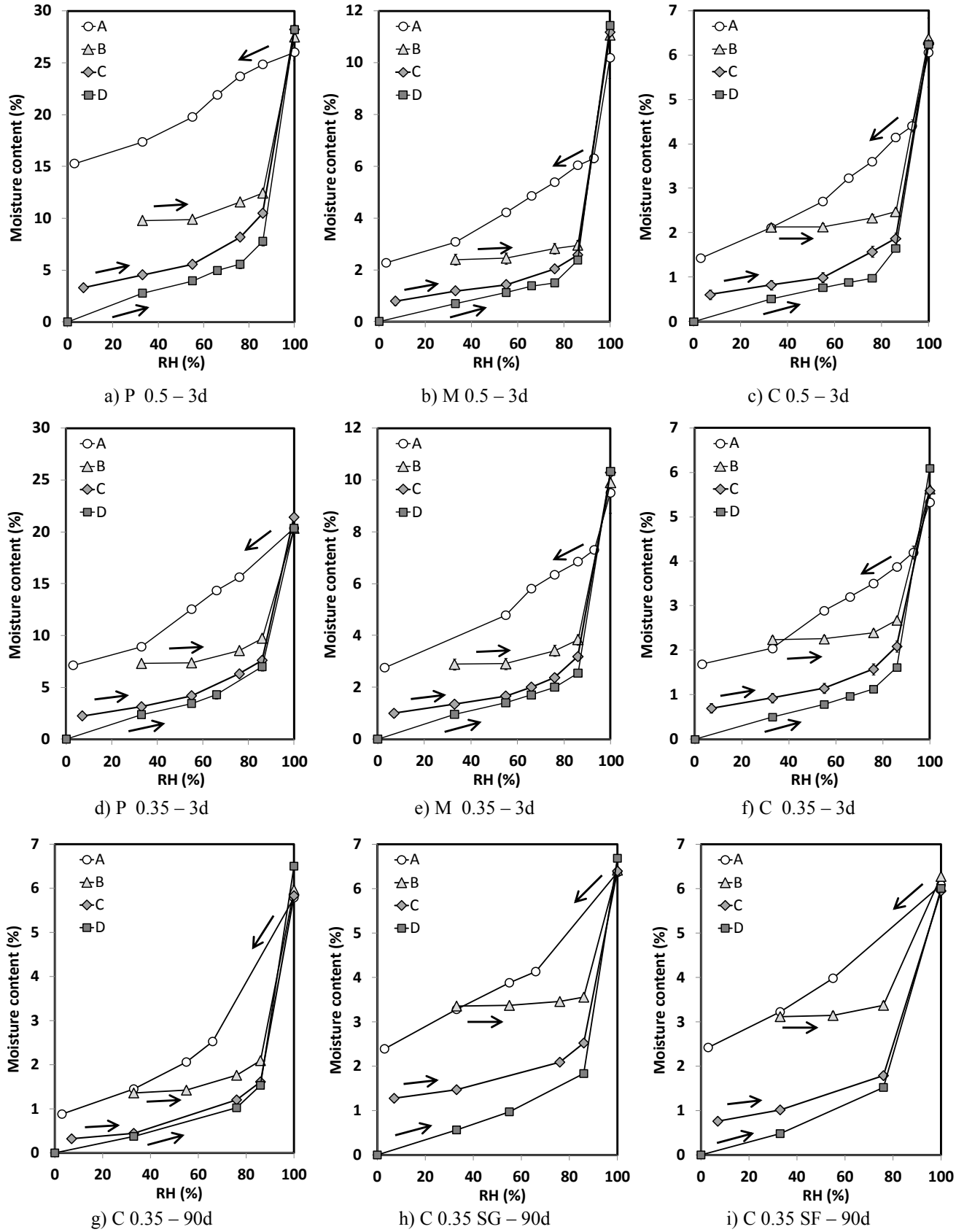

Figure 8 Equilibrium moisture content for pastes, mortars and concretes subjected to conditioning regimes shown in Fig. 1. Arrows indicate progress of drying and rewetting.

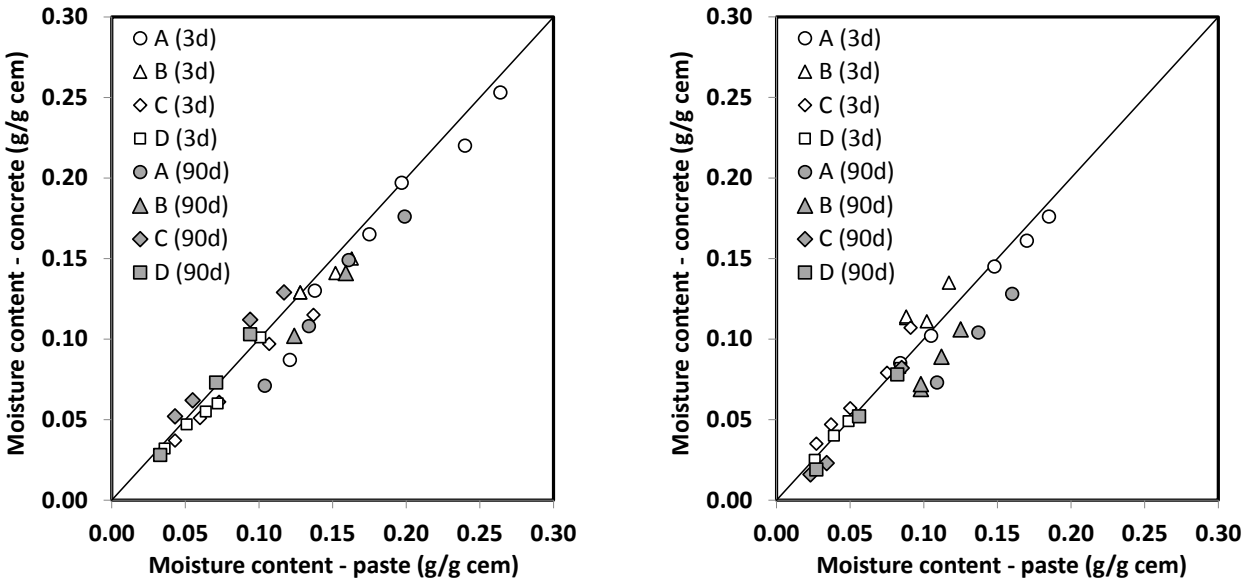

a) Water/Binder = 0.50 b) Water/Binder = 0.35

Figure 9 Comparison between moisture content for pastes and concretes at various conditioning stages. Moisture content is normalised to cement content.

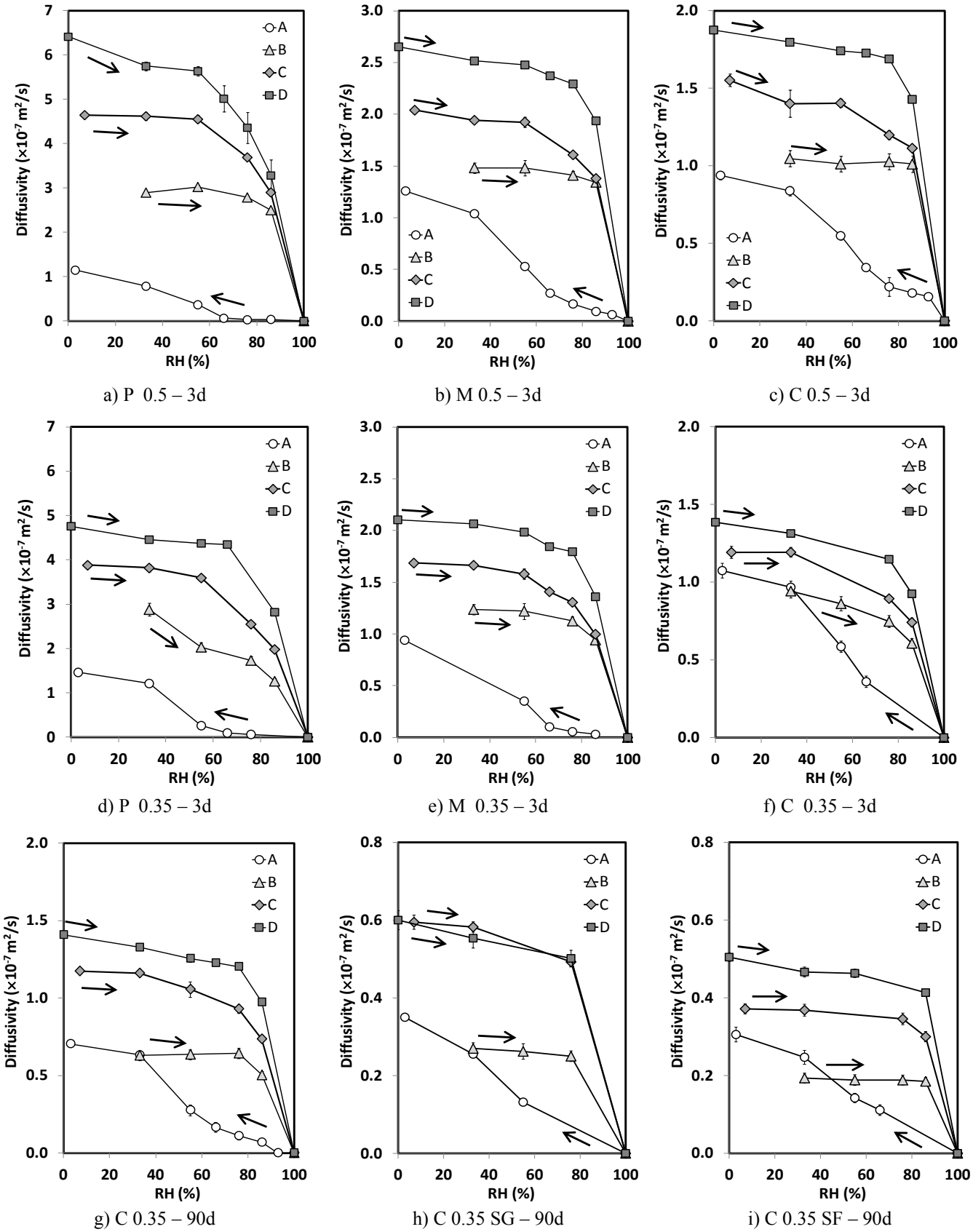

Figure 10 Effect of drying and rewetting on the diffusivity of pastes, mortars and concretes.

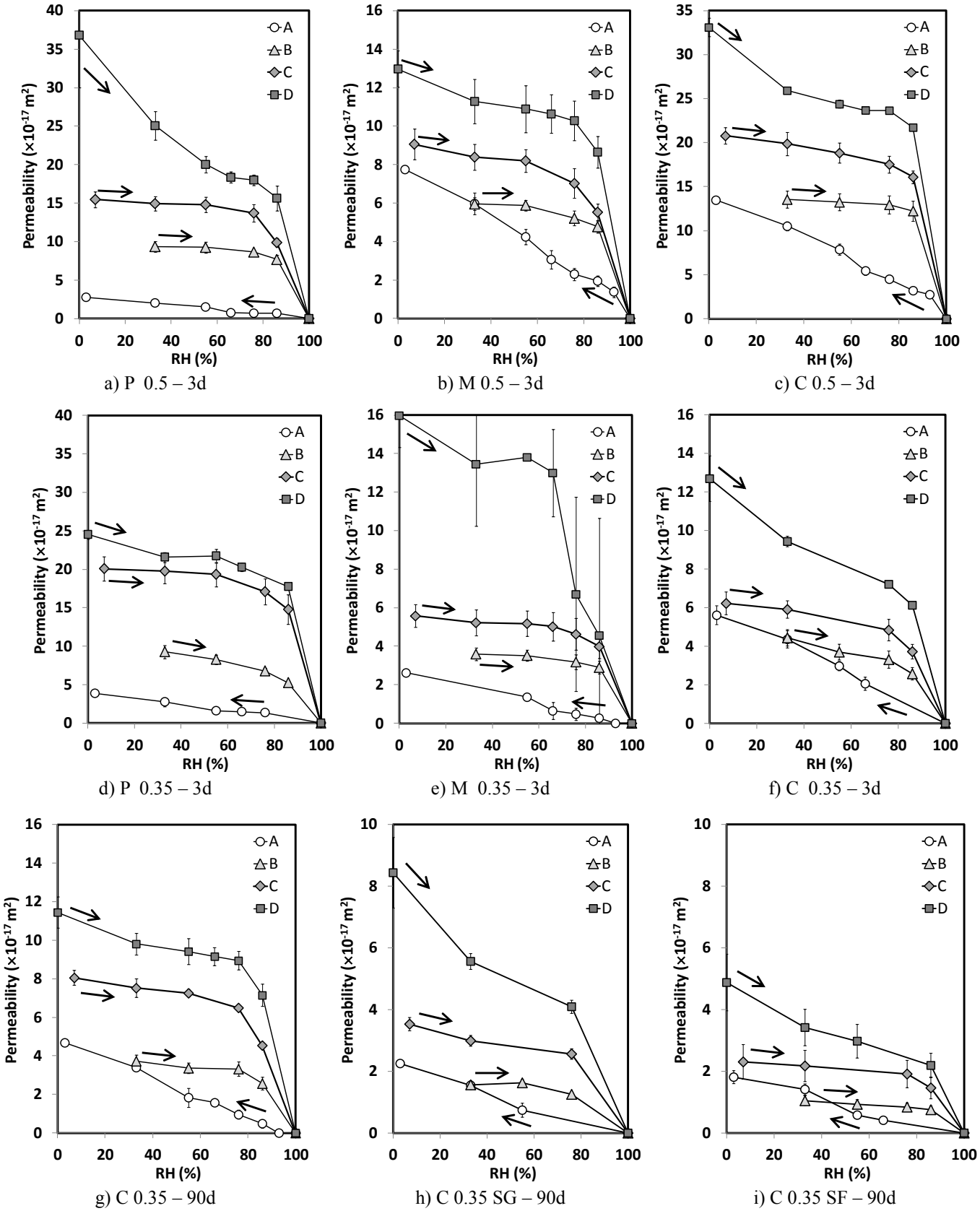

Figure 11 Effect of drying and rewetting on the permeability of pastes, mortars and concretes.

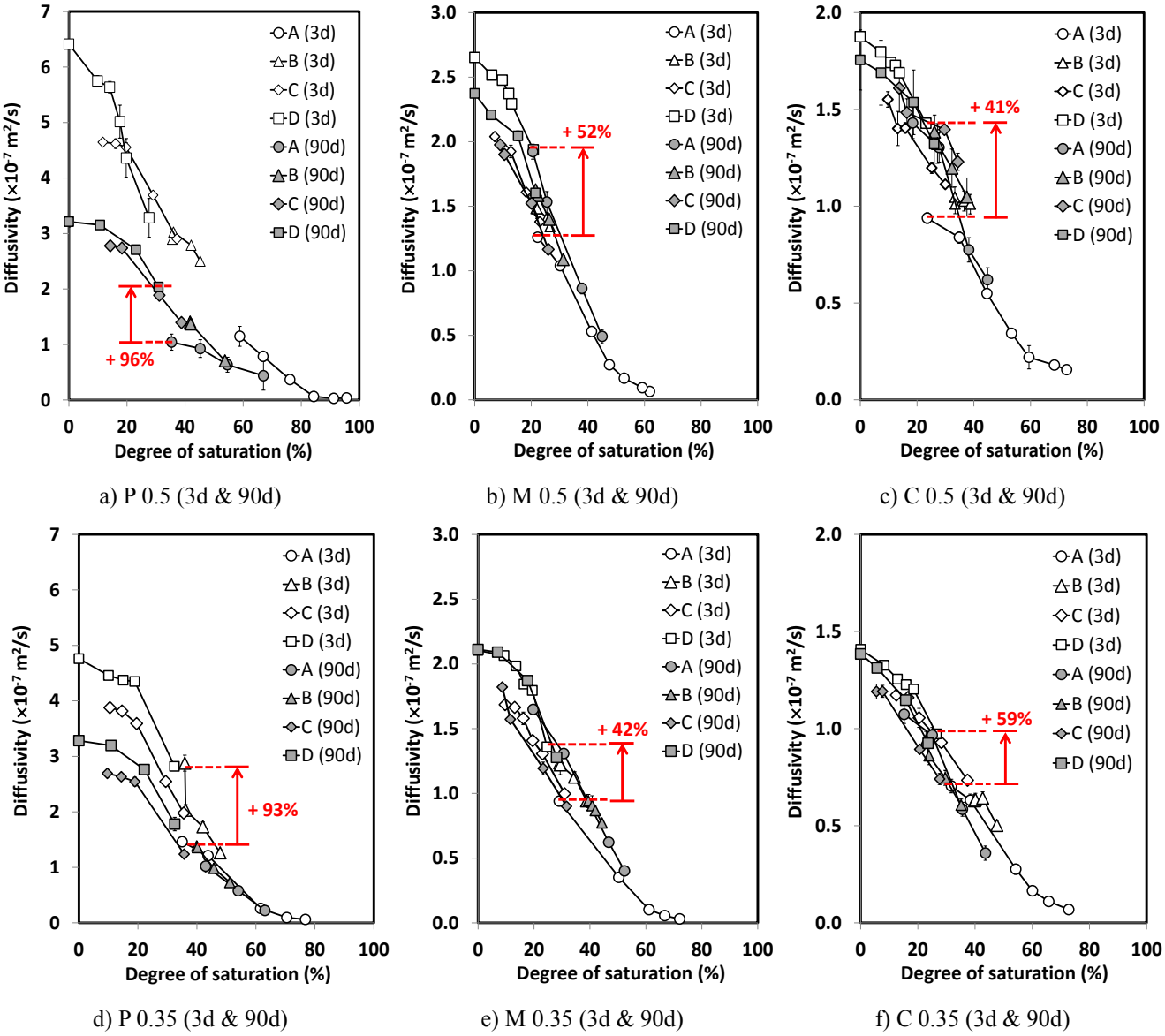

a) P 0.5 (3d & 90d) b) M 0.5 (3d & 90d) c) C 0.5 (3d & 90d)

d) P 0.35 (3d & 90d) e) M 0.35 (3d & 90d) f) C 0.35 (3d & 90d)

Figure 12 Correlation between diffusivity and degree of saturation for pastes, mortars and concretes subjected to drying and rewetting. Arrows indicate maximum difference (%) in transport property between gently and severely dried samples when measured at equal moisture content.

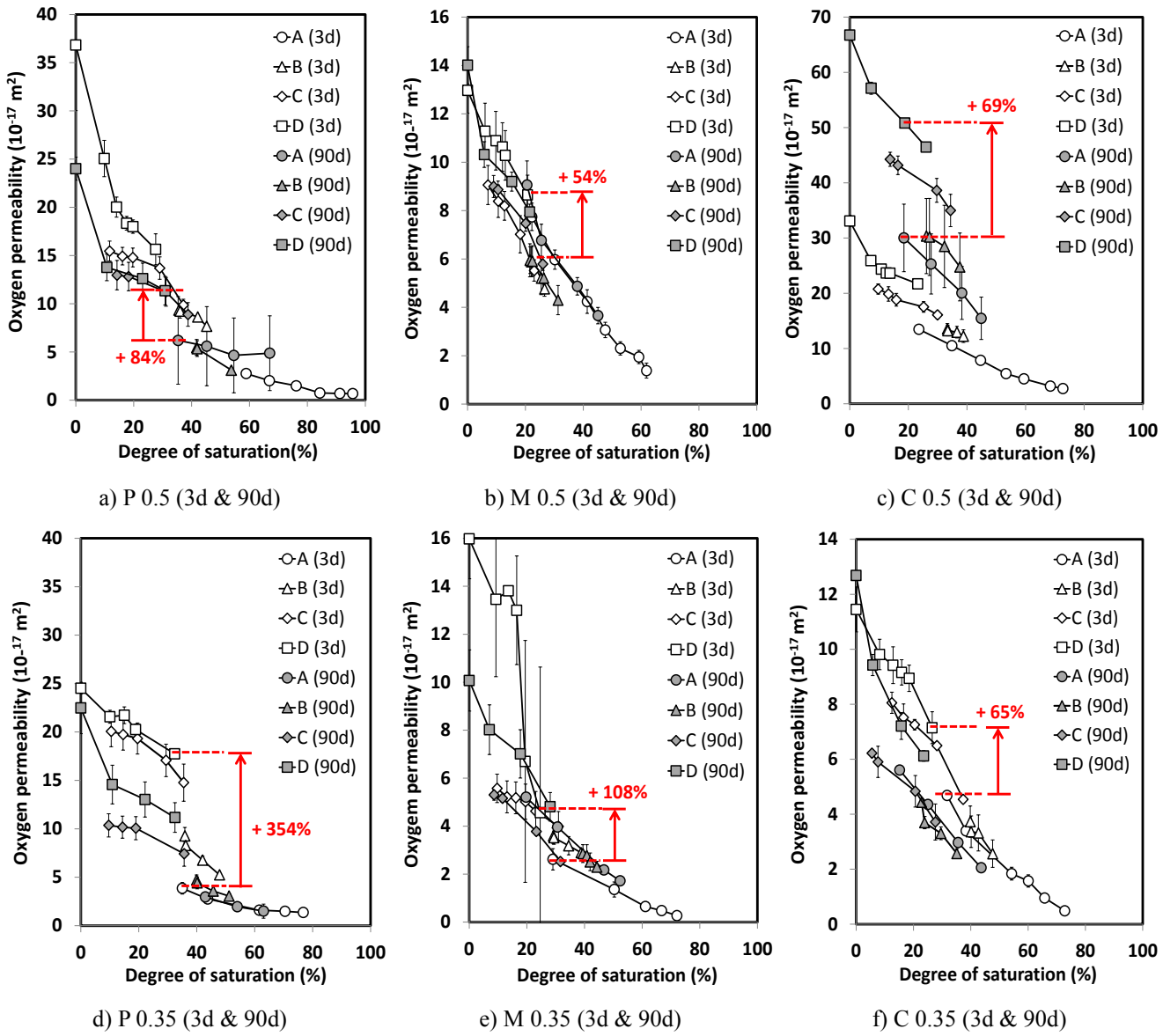

a) P 0.5 (3d & 90d) b) M 0.5 (3d & 90d) c) C 0.5 (3d & 90d)

d) P 0.35 (3d & 90d) e) M 0.35 (3d & 90d) f) C 0.35 (3d & 90d)

Figure 13 Correlation between permeability and degree of saturation for pastes, mortars and concretes subjected to drying and rewetting. Arrows indicate maximum difference (%) in transport property between gently and severely dried samples when measured at equal moisture content.

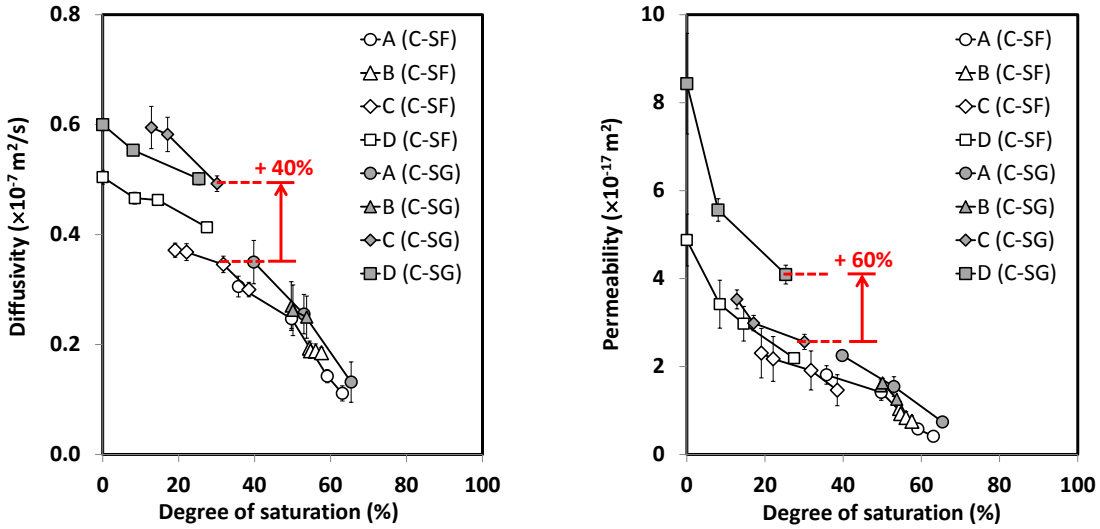

a) Diffusivity b) Permeability

Figure 14 Correlation between transport properties and degree of saturation for concretes containing silica fume (C-SF) and ground granulated blastfurnace slag (C-SG) subjected to drying and rewetting.

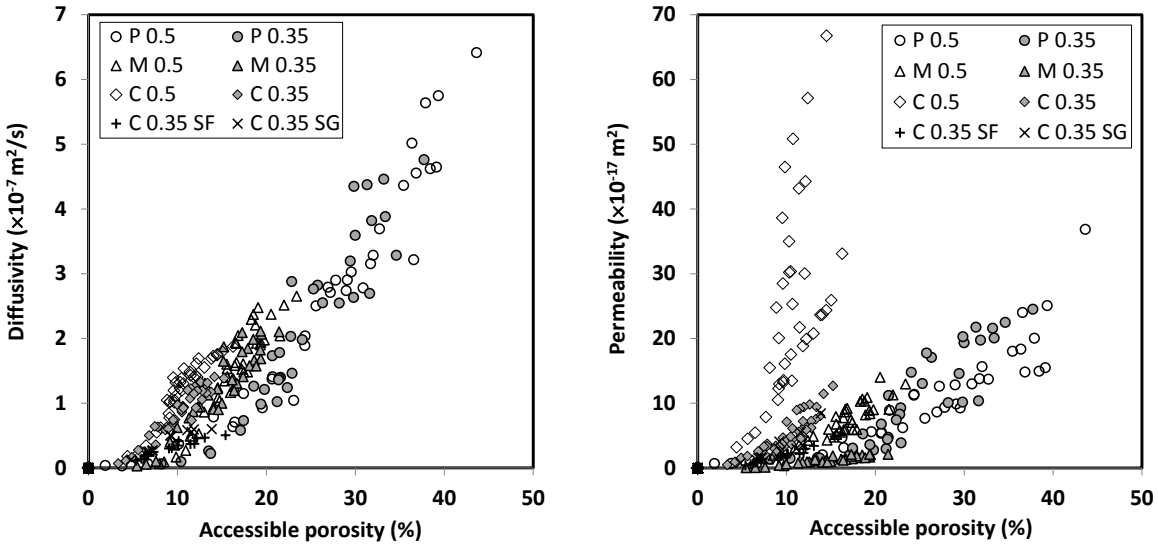

a) Diffusivity b) Permeability

Figure 15 Correlation between gaseous transport properties and accessible porosity for all samples, curing ages and conditioning regimes tested in this study.

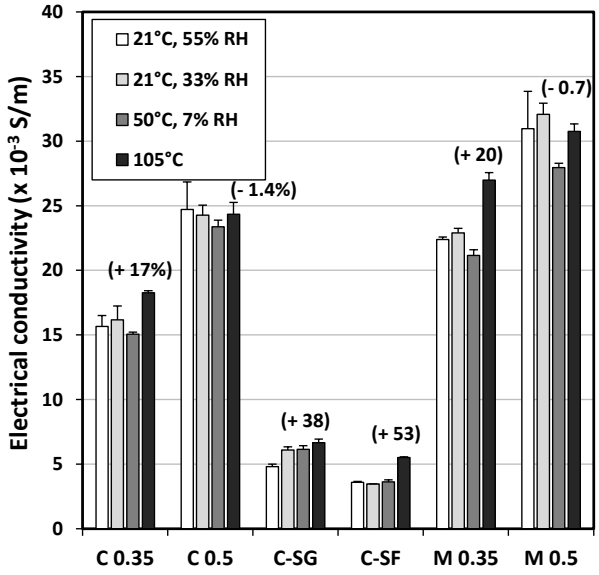

a) Electrical conductivity (90d)

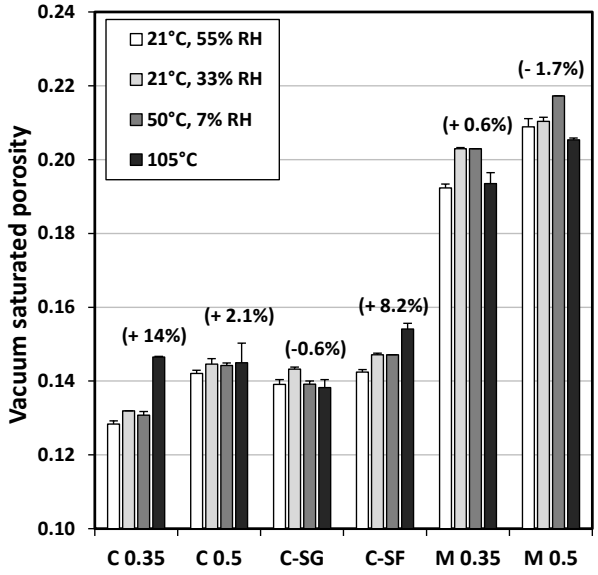

b) Porosity (90d)

Figure 16 Electrical conductivity and total porosity after drying and vacuum saturation. Numbers in brackets represent percentage difference between 105°C and 21°C 55% RH.